J. Fluid Mech. (2007), *vol.* 583, *pp.* 229–272.
doi:10.1017/S0022112007006179 Printed in the United Kingdom

Secondary instability of crossflow vortices: validation of the stability theory by direct numerical simulation

GIUSEPPE BONFIGLI AND MARKUS KLOKER

Institut für Aerodynamik und Gasdynamik, Universität Stuttgart, Pfaffenwaldring 21, D-70550 Stuttgart, Germany

(Received 17 July 2006 and in revised form 1 February 2007)

Detailed comparison of spatial direct numerical simulations (DNS) and secondary linear stability theory (SLST) is provided for the three-dimensional crossflow-dominated boundary layer also considered at the DLR-Göttingen for experiments and theory. Secondary instabilities of large-amplitude steady and unsteady crossflow vortices arising from one single primary mode have been analysed. SLST results have been found to be reliable with respect to the dispersion relation and the amplitude distribution of the modal eigenfunction in the crosscut plane. However, significant deviations have been found in the amplification rates, the SLST results being strongly dependent on the necessarily simplified representation of the primary state. The secondary instability mechanisms are shown to be local, i.e. robust with respect to violations of the periodicity assumption made in the SLST for the wall-parallel directions. Perturbations associated with different local maxima of the spanwise periodic eigenfunctions develop independently from each other interacting only with the primary vortices next to them. Characteristic structures induced by different secondary instability modes have been analysed and an analogy with the Kelvin–Helmholtz instability mechanism has been highlighted.

1. Introduction

Significant progress has been made in the past decade in work on transition in three-dimensional crossflow (CF) dominated boundary layers. Starting from the available characterization of primary instabilities (see Reed & Saric 1989; Bippes 1999), a secondary instability of large-amplitude CF vortices could be identified theoretically (Balachandar, Streett & Malik 1992; Malik & Chang 1994; Malik *et al.* 1999; Koch *et al.* 2000), numerically (Högberg & Henningson 1998; Wassermann & Kloker 2002, 2003; Wintergerste 2002), and experimentally (Bippes 1999; Kawakami, Kohama & Okutsu 1999; White *et al.* 2001; Chernoray *et al.* 2005; White & Saric 2005). With some limitations to be detailed in the following, the successive growth of primary and secondary instabilities has been recognized as the two fundamental steps in the transition process. Both experimental and numerical evidence indicates that the laminar–turbulent breakdown readily follows the onset of the explosive convective secondary instability (see also the review by Saric, Reed & White 2003).

The theoretical model for the secondary instability mechanism is provided by the secondary linear stability theory (SLST) developed by Balachandar *et al.* (1992), Malik & Chang (1994), Malik *et al.* (1999) and Koch *et al.* (2000). The stability of three-dimensional boundary layers nonlinearly deformed by primary CF vortices is investigated with respect to infinitesimal perturbations. The unperturbed state

(primary state) is assumed to be invariant in the direction of the primary-vortex axis and to be steady in a proper Galilean reference system. Both assumptions are approximated well when only one steady or unsteady primary mode is excited (steady and unsteady fundamental cases), in which case the primary state is characterized by stationary or travelling CF vortices resulting from the superposition of the excited mode and its spanwise superharmonics. In the unsteady case, the CF vortices drift in a spanwise direction with the phase velocity of the generating mode, which is also the phase velocity of its superharmonics, and are steady in a reference system moving with that same velocity. The case in which different steady modes are superposed to produce an array of non-identical steady CF vortices (steady CF packet, see Wassermann & Kloker 2003) or even a single isolated vortex (see Radeztsky, Reibert & Saric 1999) also fits the assumptions mentioned. Cases where at least two modes with different phase velocities simultaneously achieve relevant amplitudes (non-fundamental cases) are *a priori* not covered by the SLST (see, e.g. Bonfigli & Kloker 1999).

By assuming the infinitesimal secondary perturbation to be a harmonic wave in the direction of the CF-vortex axes, linearizing the Navier–Stokes equations, and imposing homogeneous boundary conditions for the perturbation at the wall and in the free stream, the stability analysis reduces to an eigenvalue problem governed by two-dimensional partial differential equations in the two remaining spatial directions. Only results for spanwise periodic fundamental cases are available in the literature (see Malik & Chang 1994; Koch *et al.* 2000; Janke & Balakumar 2000), where Fourier expansions are introduced for the discretization of the eigenvalue problem in the spanwise direction (Floquet theory). The distinction between the temporal and spatial approaches holds analogously to the primary stability problem. Koch *et al.* (2000) showed that a generalization of the Gaster transformation used by Malik *et al.* (1999) holds exactly for the infinite-span configurations with spanwise periodic primary state.

The characterization of secondary unstable modes with respect to the dispersion relation, amplification rates and the amplitude distribution of the eigenfunctions for the steady fundamental case is well established and will not be detailed here. We follow the terminology of Koch *et al.* (2000) and indicate high-frequency modes connected to the spanwise shear layer at the updraft side of the primary vortices as type I modes (z-mode in Malik *et al.* 1999), high-frequency modes connected to the wall-normal shear layer on top of the primary vortices as type II modes (y-mode in Malik *et al.* 1999), and the low-frequency modes developing close to the wall underneath the primary vortices as type III modes. The convective character of secondary instabilities has been verified by Wassermann & Kloker (2002) by means of DNS and later, theoretically, by Koch (2002).

Comparisons between SLST, experimental results and DNS have always been qualitative and limited to the steady fundamental state. Because of the lack of detailed experimental and numerical results, comparisons were possible only with respect to the characteristic frequencies and the crosscut amplitude distributions for unstable secondary modes. Agreement was found in all cases for the development of type I and type III modes, but some inconsistencies were found with respect to the role of type II modes. These often attained the largest amplification rates in SLST computations, in particular in the high-frequency range (Malik *et al.* 1999; Janke & Balakumar 2000; Koch *et al.* 2000), but were not observed in most experimental investigations (Kawakami *et al.* 1999; White *et al.* 2001) or DNS (Högberg & Henningson 1998; Wassermann & Kloker 2002). Type II modes were detected by Wassermann & Kloker (2002) and White & Saric (2005) in scenarios with subcritical primary steady perturbations, but a significant disagreement was also observed by White & Saric

between the large amplifications provided for those modes by the SLST and the moderate amplitudes they effectively achieved with respect to type I modes. Both Malik *et al.* (1999) and White & Saric (2005) justified the inconsistency on the basis of receptivity considerations. Indeed, the energy content of perturbations exciting secondary modes in experiments or DNS might be lower for very high frequencies, for which type II modes dominate, than for lower frequencies, for which type I and type III modes undergo larger amplification. If no doubt remains that secondary instabilities may be active in real flows as foreseen by the SLST, a quantitative validation of SLST results is still missing and might help to answer the open questions connected to type II modes.

In all available DNS (Högberg & Henningson 1998; Wassermann & Kloker 2002, 2003), and in general under the assumption of infinite span, periodicity is given in the spanwise direction and spatial amplification is restricted to the downstream direction. On the contrary, within the SLST, amplification and periodicity are usually prescribed along the vortex-oriented coordinates, in the direction of the vortex axis and normal to it, respectively. This introduces a potential discrepancy, which is not necessarily negligible even when the physically motivated assumptions of the theory are fulfilled. Connected to this point is also the question of whether the periodicity of primary and secondary perturbation is a necessary precondition for the development of the instability. Both issues are of major relevance in determining whether SLST results may be extrapolated to realistic flow configurations, which, of course, may not be expected to be perfectly periodic in any direction. Koch *et al.* (2000) considered detuned modes in their SLST Floquet-analysis, thus loosening the periodicity requirements on the secondary perturbation, but not on the primary flow. Furthermore, they also solved the spatial problem imposing amplification along the chord of their flat plate, which did not coincide with the direction of the primary-vortex axes. Both aspects are connected to the issues mentioned above, but no conclusions have been drawn in that regard. According to Koch *et al.* (2000), detuned modes may achieve moderately larger amplification rates than tuned modes. Qualitative similarity between eigenfunctions of tuned and subharmonic secondary modes has been observed by Balachandar *et al.* (1992).

The visualization of the flow fields resulting from the growth of secondary unstable perturbations was attempted by Balachandar *et al.* (1992) and Malik & Chang (1994) by superposing finite-amplitude eigenfunctions onto the corresponding steady primary state for a rotating-disk flow and a swept Hiemenz flow, respectively. Balachandar *et al.* (1992) conjectured the development of secondary vortices at the side of the primary one, whereas Malik & Chang (1994), who considered a type II mode, observed corotating secondary vortices on top of it. Detailed and conclusive visualizations of the actual flow field have been provided by Wassermann & Kloker (2002, 2003) on the basis of DNS results for both steady and unsteady fundamental cases, and for the steady CF-packet case. In computations, where secondary instabilities were excited by multi-frequency pulse-like perturbations, they found short trains of finger-like vortical structures developing at the side of the primary vortex, in a region where type I eigenfunctions achieve their maximum amplitudes. The attribution of the secondary structures to large-amplitude type I modes was then a matter of course. Type III modes were observed by different authors for the steady fundamental case (Koch *et al.* 2000; Högberg & Henningson 1998; Wassermann & Kloker 2002, 2005), but the corresponding structures were never documented.

The only available results for unsteady fundamental cases are experimental results by Lerche (1997) and DNS by Wassermann & Kloker (2003). Balachandar *et al.*

(1992) and Koch *et al.* (2000) developed SLST codes capable of considering the unsteady fundamental case, but provided no results. Secondary modes analogous to type I modes from the steady fundamental case, but now moving with the primary vortices, were documented by Wassermann & Kloker (2003).

An answer to the question of whether the secondary instability mechanism observed in the fundamental steady or unsteady cases may apply also to non-fundamental cases is still missing. Transition scenarios characterized by the simultaneous perturbation of steady and unsteady primary modes have been investigated by Bippes (1999) experimentally, by Hein (2004) by means of highly resolved PSE, and by Wintergerste (2002) by means of temporal DNS. Even if Bippes (1999) measured high-frequency perturbations reminiscent of type I modes in regions with highly deformed primary profiles, a clear identification of secondary instabilities could not be achieved.

The development of isolated secondary-structure trains in the DNS of the fundamental cases by Wassermann & Kloker (2002, 2003) suggests a local behaviour of secondary perturbations in the streamwise direction, in the sense that periodicity of the flow in that direction, as assumed by the SLST, may not be necessary for secondary growth. Further investigation of the characteristics of the secondary modes and of the generating mechanism might help to clarify this point which is also relevant with respect to the question of whether the development of secondary instabilities might be possible in non-fundamental scenarios. In such cases, indeed, streamwise invariance of the primary state is not granted, and secondary instabilities as predicted by the SLST could develop only if, being a local phenomenon, they were non-sensitive to that point.

Starting from the results discussed above, the following aspects of secondary instabilities in the fundamental scenarios will be addressed in the present paper:

(i) *quantitative* validation of the SLST by comparison with DNS results;

(ii) clarification of the disagreement between DNS and SLST with respect to the role of type II modes;

(iii) investigation of the influence of the choice of the directions of exponential growth and periodicity onto the instability behaviour;

(iv) investigation of the consequences induced on the SLST results by the assumption of periodicity in the wall-parallel directions;

(v) documentation of vortical structures associated to single type I and type III modes;

(vi) discussion and interpretation of the secondary instability mechanism.

The numerical procedures for DNS and SLST are presented in § 2, while §§ 3 and 4 provide a characterization of the three-dimensional base flow and of the primary states for the considered steady and unsteady fundamental scenarios. Validation of the SLST by comparison with the DNS is discussed in §§ 5 and 6, where also open questions relative to the role of type II modes and to the influence of the choice of the periodicity and exponential-grow directions are answered. The flow field and the vortical structure associated to single large-amplitude secondary modes are documented in § 7. An interpretation of the instability mechanism on the basis of an analogy with the inviscid Kelvin–Helmholtz instability of the plane mixing layer (see Drazin & Reid 2004) is proposed and verified in § 8.

2. Notations and basics of the numerical methods

2.1. *Reference systems and non-dimensionalization*

The reference systems considered for the formulation of the numerical procedures and for post-processing are sketched in figure 1. Only boundary layers developing

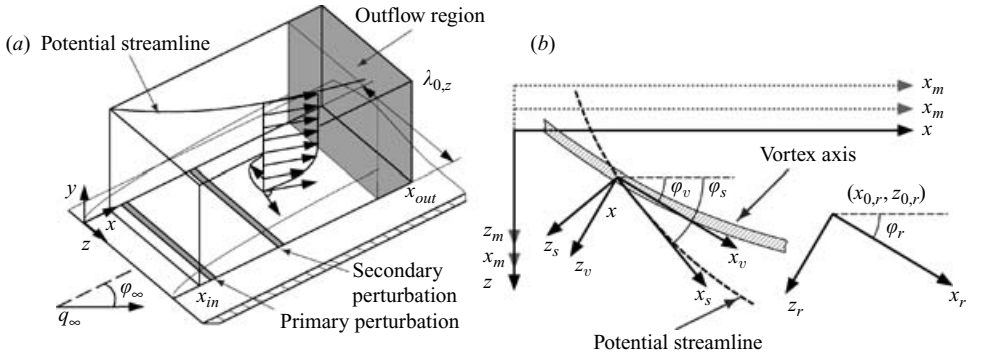

FIGURE 1. (*a*) Integration domain and (*b*) reference systems. The sign convention for angles is such that for the configuration displayed in (*b*), φ_s, φ_r and φ_v are positive.

on a flat plate will be considered and the origin of all systems lies on the plate surface. In all cases, the y-axis is normal to the plate surface and points into the flow. The governing equations for the DNS are formulated in the plate-oriented reference system (x, y, z), with the origin lying on the plate leading edge, and the x-axis normal to it. The streamwise oriented reference system (x_s, y, z_s) is defined at every downstream position requiring the x_s-axis to be tangent to the edge streamline. The vortex-oriented reference system (x_v, y, z_v) is considered for the SLST analysis of the steady fundamental case. It is defined at every chord position requiring the x_v-axis to be normal to the wave vector of the primary perturbation, resulting from the primary linear stability theory (PLST) at that position. The arbitrarily rotated reference system (x_r, y, z_r) is used for post-processing. Each time, the position of its origin $(x_{0,r}, z_{0,r})$ in the plate-oriented reference system and the rotation angle φ_r are explicitly assigned. The moving reference system (x_m, y, z_m) is relevant for the unsteady fundamental cases. It is defined analogously to the plate-oriented system (x, y, z), but translates in z with constant velocity c_m equal to the phase velocity of the primary perturbations in that direction. The moving vortex-oriented reference system $(x_{v,m}, y, z_{v,m})$ and the moving rotated reference system $(x_{r,m}, y, z_{r,m})$ (not shown in figure 1) are defined analogously to (x_v, y, z_v) and (x_r, y, z_r), but translate in z in the same way as (x_m, y, z_m). Correspondingly, the coordinates $(x_{0,r,m}, z_{0,r,m})$ of the origin of the $(x_{r,m}, y, z_{r,m})$ are given with respect the moving system (x_m, y, z_m).

Components of the velocity and vorticity vectors in the plate-oriented reference system are (u, v, w) and $(\omega_x, \omega_y, \omega_z)$, respectively. The letters α and γ are used to indicate wavenumbers along the wall parallel directions x and z. Quantities referring to different reference systems are marked by the corresponding subscripts (for example u_s). The sign for angles and vorticity components is defined according to the left-hand rule.

Using an asterisk to indicate dimensional quantities, flow field and governing equations are made non-dimensional by means of the reference length $L^* = 0.1\,\mathrm{m}$, of the x-component of the free-stream velocity $u^*_\infty = 14\,\mathrm{m\,s^{-1}}$ and of the constant density $\rho^* = 1.225\,\mathrm{kg\,m^{-3}}$. The non-dimensional kinematic viscosity ν is equal to the inverse of the Reynolds number $Re = L^* u^*_\infty / \nu^* = 1/\nu = 92\,000$.

Non-dimensionalization with the local edge velocity $u_{e,s}$ is normally used for post-processing. For the general flow quantity f, the following notation is used:

$$\tilde{f} = \frac{f}{u_{e,s}}. \tag{2.1}$$

2.2. *DNS code*

The DNS procedure used for the present paper is based on Kloker (1993), Müller (1995), Wassermann & Kloker (2002, 2003) and Bonfigli (2006). According to the so-called spatial approach, the development of a three-dimensional boundary layer along an infinite-span flat plate with given sweep is simulated by solving the full three-dimensional unsteady incompressible Navier–Stokes equations inside the rectangular domain shown in figure 1. The oncoming flow and the inviscid flow far outside of the boundary layer are assumed to be steady and spanwise invariant (quasi three-dimensional flow). Flows with streamwise pressure gradients can be considered by imposing a non-constant edge velocity $u_{e,s}$. In addition, spanwise periodic steady and unsteady perturbations may be introduced through suction and blowing within one or more strips on the wall surface (see figure 1). Single primary and secondary unstable modes of the boundary layer may be perturbed by properly defining the time development and the spatial distribution of the wall perturbation. Indeed, we consider only perturbations which are periodic both in time and in the spanwise direction and indicate with $\omega_0 = 2\pi/T_0$ and $\gamma_0 = 2\pi/\lambda_{0,z}$ the fundamental angular frequency and the spanwise wavenumber, respectively.

A vorticity–velocity formulation of the Navier–Stokes equations is used and the numerical procedure relies on the decomposition of the flow quantities into the base flow, i.e. the steady spanwise invariant solution of the unperturbed problem, and perturbation flow, i.e. the deviation from the base flow as a consequence of suction and blowing at the wall. For the general flow quantity f we have $f(t, x, y, z) = f_b(x, y) + f'(t, x, y, z)$, where f_b and f' are the base flow and the perturbation, respectively. Of course, no linearization is introduced through this splitting, which, on the other hand, allows the imposition of different optimal boundary conditions for base and disturbance flow, as well as the separate manipulation of any of the two flow components, as will be seen below.

Fourth-order standard finite differences on an equidistant orthogonal grid are used in downstream (x) and wall-normal directions (y) for the computation of the base flow. The solution is converged by a fictive time integration using low-order time-marching schemes. Spatial discretization for the perturbation flow is obtained by combining Fourier expansion in the z-direction with sixth-order compact finite differences for the downstream and wall-normal directions. While the step size in the streamwise direction (Δx) is constant, that in the wall-normal direction (Δy) may be varied blockwise, progressively doubling for increasing distance from the wall. Integration in time is achieved by a fourth-order Runge–Kutta scheme. Reflection at the outflow boundary is avoided by suppressing oncoming (vorticity) perturbations in a short region upstream of the actual outflow boundary.

A thorough description of the governing equations and of the boundary conditions for the numerical algorithm is provided by Wassermann & Kloker (2002, 2003). They also provided a validation of the procedure with respect to the growth and nonlinear saturation of steady and unsteady primary modes. The missing validation for the growth of secondary instabilities is provided in §§ 5 and 6.

Deviating from the standard procedure, linearized simulations with spanwise periodic base flow ($f_b = f_b(x, y, z)$) have been carried out in some cases, in order to reproduce the simplified SLST flow field in the DNS computation. Base flow and perturbation had then the same spanwise wavelength in the z-direction and the former was defined (not computed) following the procedure used to determine the primary state for SLST computations (see § 4.2). Linearization has been carried out with respect to the perturbation flow and, of course, does not affect the nonlinear

interaction between secondary perturbation and primary state, represented by the base flow.

2.3. *SLST code*

The numerical procedure for the SLST analysis has been implemented by Messing (2004) following the normal-velocity–normal-vorticity formulation of the stability problem as developed by Koch *et al.* (2000). Referring to the vortex-oriented (fixed or moving) reference system, the primary state is steady, constant over x_v and periodic in z_v (array of elongated CF vortices). A secondary mode is an amplified or damped harmonic wave in time (temporal approach), a neutral harmonic wave in x_v and generically periodic in z_v (Floquet theory), which implies that secondary perturbations present a two-dimensional amplitude distribution in the crosscut plane (y, z_v). For the general flow, quantity f of the steady fundamental case holds, $f(t, x_v, y, z_v) = \dot{f}(x_v, y, z_v) + \ddot{f}(t, x_v, y, z_v)$, where $\dot{f}$ and $\ddot{f}$ represent the primary state and the secondary perturbation, respectively. Moreover, the expression

$$\ddot{f}(t, x_v, y, z_v) = 2\,\mathrm{Re}[\hat{\ddot{f}}(y, z_v)\exp(\mathrm{i}(\alpha_v x_v - \omega t))], \quad \alpha_v \in \mathbb{R},\ \omega \in \mathbb{C}, \tag{2.2}$$

holds for $\ddot{f}$, where the complex-valued function $\hat{\ddot{f}}$ is z_v-periodic and Re is the real-part operator. We consider only tuned cases where primary and secondary perturbations possess the same periodicity in the z_v-direction, which, according to the results of § 6.2, represents no limitation on the analysis. For every fixed α_v, the stability analysis reduces to an eigenvalue problem, where ω is the eigenvalue and $\hat{\ddot{f}}$ is the eigenfunction. The amplitude distribution of the latter in the crosscut plane (x_v, z_v) corresponds then to the well known two-dimensional amplitude distributions for secondary perturbations. The formulation for the unsteady fundamental case is completely analogous, the only difference being that all quantities are expressed as functions of the coordinates in the moving system $(x_{v,m}, y, z_{v,m})$.

Discretization of the partial differential equations governing the eigenvalue problem is achieved combining fourth-order compact finite differences in the wall-normal direction with Fourier expansions in the z_v-direction. The full spectrum of the resulting discretized problem is computed for one α_v-value using standard numerical libraries. A Wieland-type iteration as implemented by Koch *et al.* (2000) is then used for tracking relevant eigenmodes while varying various parameters of the stability problem.

The characteristics of spatially developing secondary perturbations are evaluated on the basis of the results from the temporal analysis implemented in the numerical code. According to the spatial approach of the SLST the expression

$$\ddot{f}(t, x_v, y, z_v) = 2\mathrm{Re}[\hat{\ddot{f}}(y, z_v)\exp(\mathrm{i}(\alpha_v x_v - \omega t))], \quad \alpha_v \in \mathbb{C},\ \omega \in \mathbb{R}, \tag{2.3}$$

holds for the general quantity $\ddot{f}$ of the secondary perturbation in the steady fundamental case. The corresponding eigenvalue problem is achieved by imposing ω and considering α_v as an eigenvalue. Koch *et al.* (2000) showed that, indicating with T and S quantities from the temporal (equation (2.2)) and spatial approach (equation (2.3)), respectively, the following identities hold almost exactly:

$$\omega_S = \mathrm{Re}(\omega_T), \tag{2.4a}$$

$$\mathrm{Re}(\alpha_{v,S}) = \alpha_{v,T}, \tag{2.4b}$$

$$\hat{\ddot{f}}_S(y, z_v) = \hat{\ddot{f}}_T(y, z_v), \qquad \forall\, y,\ z_v, \tag{2.4c}$$

$$\mathrm{Im}(\alpha_{v,S}) = -\frac{\mathrm{Im}(\omega_T)}{c_{gr}}, \qquad c_{gr} = \frac{\partial \mathrm{Re}(\omega_T)}{\partial \alpha_{v,T}}. \tag{2.4d}$$

They correspond to a generalization of the Gaster transformation for the PLST in two-dimensional boundary layers and provide a one-to-one correspondence between secondary modes from the spatial and the temporal approach.

A detailed description of the numerical code for the SLST analysis is provided by Messing (2004), who also achieved a verification of the results by comparison with data by Koch *et al.* (2000). Thereby an ambiguity in the notation of the coefficients given by the latter authors could be clarified (see Koch 2002, footnote on p. 102). Quantitative validation by comparison with DNS is provided in §§ 5 and 6, where also the validity of the Gaster transformation (2.4*a*) is confirmed.

2.4. *Fourier analysis*

Fourier expansion of the flow quantities in time is a fundamental tool in order to identify both primary and secondary perturbations in the DNS flow field. Indicating by f the generic flow quantity, we always consider expansions of the type

$$f(t, x, y, z) = \sum_{h=-\infty}^{\infty} \hat{f}_{(h)}(x, y, z) \exp(\mathrm{i}h\omega_0 t). \tag{2.5}$$

In some cases, modal amplitudes of harmonics $h > 0$ may be doubled to take into account the contribution of components $h < 0$. To this purpose, we introduce the notation

$$f_{(0)} = \left|\hat{f}_{(0)}\right|, \qquad f_{(k)} = 2\left|\hat{f}_{(h)}\right|, \quad \forall h > 0. \tag{2.6}$$

Moreover, $f_{(0,0)}$ is the spanwise average of the steady harmonic $f_{(0)}$.

Double Fourier transformation in time and in the spanwise direction is useful to identify primary CF modes. Index pairs (h, k), $h \geqslant 0$, are used to indicate primary modes with frequency $\omega = h\omega_0$ and spanwise wavenumber $\gamma = k\gamma_0$. Modes with positive k travel in the direction of the positive z-axis, i.e. against the crossflow.

3. Base flow

All results presented in this paper refer to the base flow of the crossflow experiment of the DLR-Göttingen by Bippes and coworkers (Müller 1990; Lerche 1997; Bippes 1999). In the experimental set-up, the three-dimensional boundary layer developed on a flat plate mounted in the wind tunnel with zero incidence and effective sweep varying between $\varphi_\infty = 42.5^\circ$ and $\varphi_\infty = 43.5^\circ$. The chord length was $L_c^* = 0.5\,\mathrm{m}$ and measurements were carried out for free-stream velocities q_∞^* between $12.5\,\mathrm{m\,s^{-1}}$ and $19\,\mathrm{m\,s^{-1}}$. A nearly constant favourable pressure gradient was induced by means of a displacement body above the plate. The pressure coefficient c_p at fixed chord positions was almost independent of q_∞^* and the infinite-span condition was approximated well.

For our numerical investigations we adopted $\varphi_\infty = 42.5^\circ$ and $q_\infty^* = 19\,\mathrm{m\,s^{-1}}$, corresponding to the parameter set considered by most authors for theoretical and numerical investigations of the DLR-experiment (Meyer 1989; Janke & Balakumar 2000; Koch *et al.* 2000; Koch 2002; Wintergerste 2002; Hein 2004). The streamwise velocity $u_{b,e}$ at the boundary-layer edge was found from the linear c_p distribution,

$$c_p = \frac{p^* - p_\infty^*}{\frac{1}{2}\rho^* q_\infty^{*\,2}} = 0.941 - 0.845\frac{x^*}{c^*} = 0.941 - 0.169\,x, \tag{3.1}$$

proposed by Meyer (1989). The spanwise component $w_{b,e}$ was constant and equal to its value at infinity. The inflow boundary was located at $x = 1$ and the corresponding boundary conditions were defined assuming a Falkner–Skan–Cooke profile matching

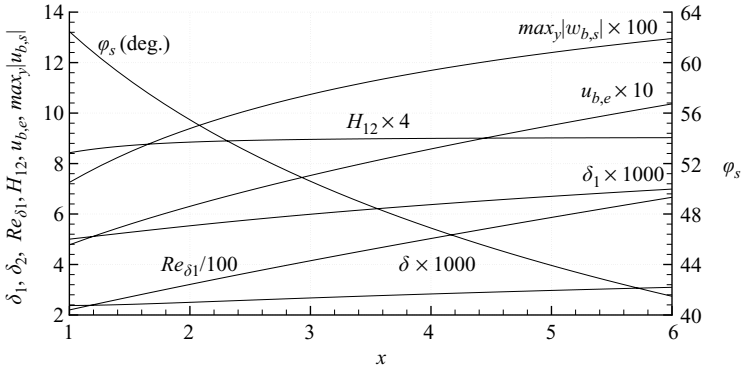

FIGURE 2. Parameters of the base flow as functions of the chord position x: edge velocity $u_{b,e}$ displacement thickness δ_1, momentum thickness δ_2, local Reynolds number $Re_{\delta 1}$, shape parameter H_{12}, local sweep angle φ_s, maximum crossflow velocity $max_y|w_{b,s}|$. All integral quantities are computed for the streamwise velocity component u_b in the plate-oriented coordinate system.

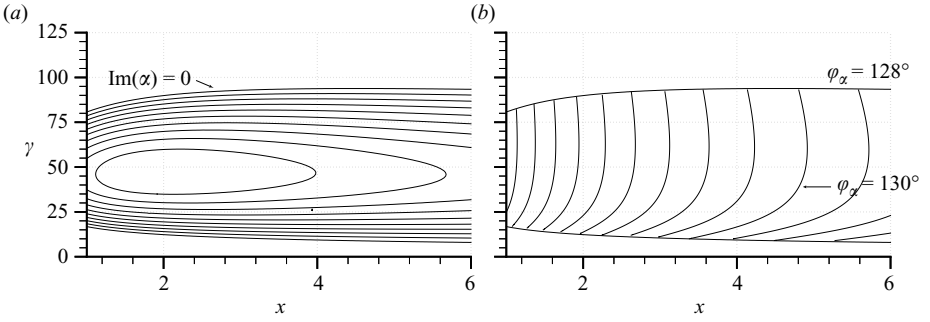

FIGURE 3. (*a*) Amplification rates Im(α) and (*b*) angle φ_α (spanned by x-axis and wave vector $[\mathrm{Re}(\alpha)\ 0\ \gamma]^T$ as functions of the spanwise wavenumber γ and of the streamwise position x for $\omega = 0$, according to the primary stability theory (spatial approach) for unstable modes. (*a*) $\mathrm{Im}(\alpha) \leqslant 0$: $\Delta = 0.25$; (b) φ_α: $\Delta = 2°$.

both the displacement thickness of the experiment and the pressure gradient resulting from (3.1).

The most relevant boundary-layer parameters computed for the streamwise velocity component u_b are plotted in figure 2 as functions of the streamwise coordinate x. Notice that even though (3.1) fits the velocity distribution of a Falkner–Skan–Cooke boundary layer with Hartree parameter $\beta_H = 2/3$ (for which the streamwise pressure gradient is constant), the resulting flow is not truly self-similar, since the constraint imposed at the inflow on the displacement thickness does not match the Falkner–Skan–Cooke solution at that chord position. The fit with a virtual leading edge, a common procedure for Blasius boundary layers, is not possible here as, in general, it is not for boundary layers with $\beta_H \neq 0$.

Amplification rates and the orientation of the wave vector for steady perturbations resulting from the primary stability theory are shown in figure 3. Because of the large sweep angle and the acceleration of the base flow in the downstream direction, CF modes are unstable at all streamwise positions. The corresponding wave vectors are nearly orthogonal to the inviscid streamline ($\varphi_\alpha \approx \varphi_s + 90°$).

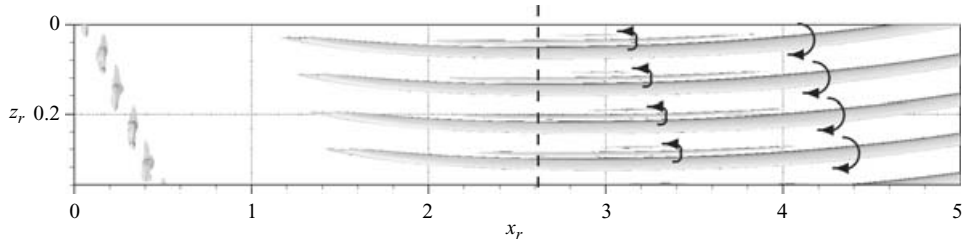

FIGURE 4. Visualization of vortical structures (λ_2-isosurfaces, $\lambda_2 = -5$) for the steady fundamental case ($x_{0,r} = 1.5$, $z_{0,r} = 0.09$, $\varphi_r = 45.86°$). Arrows indicate the rotation direction of the vortices. The dashed line shows the position of the crosscut plane of figure 5.

The base flow was computed in an extended domain ranging from $x_{in} = 1.0$ to $x_{out} = 7.43$ in a chordwise direction. The grid was equidistant and the step sizes were $\Delta x = 0.1309 \times 10^{-2}$ and $\Delta y = 0.2294 \times 10^{-3}$. When different discretizations were considered for the unsteady simulation, the available base flow was interpolated to the desired grid by means of fourth-order explicit interpolation.

4. Primary state

4.1. *DNS results*

We considered fundamental scenarios obtained by perturbing either only the steady CF mode with spanwise wavenumber $\gamma_0 = 52.4$ (i.e. wavelength $\lambda^*_{0,z} = 12\,\text{mm}$) or only the unsteady CF mode with $\gamma_0 = 52.4$ and angular frequency $\omega_0 = 6$ (i.e. frequency $f^* = (\omega u^*_\infty)/(2\pi L^*) = 133\,\text{Hz}$). In both cases, the perturbation was initiated at $x = 1.56$. Initial amplitudes were such that for $x > 3$, the streamwise perturbation $max_{t,y,z}\{u'_s\}$ achieved values between 10% and 30% of the local edge velocity $u_{e,s}$. Amplification of the primary modes was eventually suppressed by nonlinear saturation, and a periodic pattern of stationary or travelling CF vortices could be observed.

All DNS results presented in this section were computed truncating the Fourier expansion in the spanwise direction at the thirteenth superharmonic of the fundamental wavenumber γ_0 associated to the perturbed primary mode ($\gamma_{max} = 13\gamma_0$). The streamwise and the minimum wall-normal step sizes in the near-wall region were $\Delta x = 0.1309 \times 10^{-2}$ and $\Delta y_{min} = 0.1147 \times 10^{-3}$, respectively. The latter was repeatedly doubled away from the wall at $y = 0.004$, $y = 0.011$ and $y = 0.055$, and reached $\Delta y_{max} = 0.9176 \times 10^{-3}$. The upper edge of the integration domain was located at $y_e = 0.084$ and the time step was $\Delta t = 3.49 \times 10^{-4}$ (3000 time steps per period of the unsteady primary perturbation). The relatively small wall-normal step size was required to ensure a stable simulation of the primary CF vortices, which set significantly more stringent requirements than, for example, Tollmien–Schlichting waves in two-dimensional boundary layers.

4.1.1. *Steady fundamental case*

Figure 4 provides a visualization of the CF-vortex cores for the steady fundamental case by means of λ_2-isosurfaces (Jeong & Hussain 1995). The basic crossflow is from bottom to top. Small counter-rotating vortices are visible on the updraft side of the main ones; the arrows show the sense of rotation of the vortices (see also figure 5). The characteristics of the perturbed primary mode determine the periodicity of the flow in the z-direction (wavelength $\lambda_{0,z} = 0.12$) and also the orientation of the vortex axes. This becomes clear considering that we defined the orientation of the reference

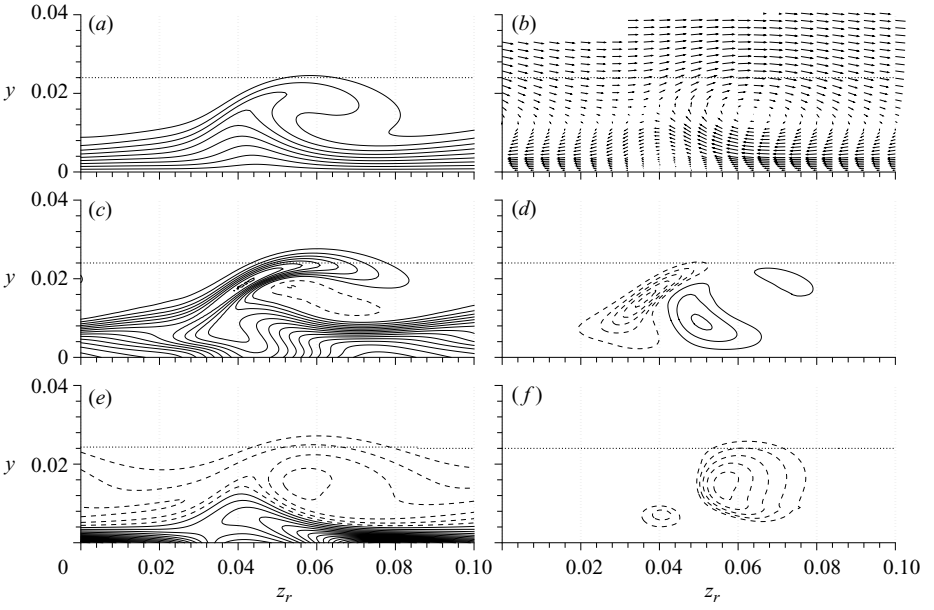

FIGURE 5. Flow field in the crosscut plane $x_r = 2.61$ of figure 4 ($x \approx 3.32$): (*a*) $\tilde{u}_r$-isocontours, $\Delta = 0.1$; (*b*) $[\tilde{w}_r, \tilde{v}_r]$-vectors; (*c*) $\partial\tilde{u}_r/\partial y$-isocontours, $\Delta = 10.0$; (*d*) $(\partial u_r/\partial z_r)/u_{b,s,e}$-isocontours, $\Delta = 10.0$; (*e*) $\tilde{\omega}_{x,r}$-isocontours, $\Delta = 2.5$; (*f*) λ_2-isocontours, $\Delta = 5.0$. Dashed lines correspond to negative values. The horizontal dotted line denotes the undisturbed boundary-layer thickness δ_s in $z_r = 0$. The variation of δ_s over the considered z_r-interval is less than 1%.

system for the visualization ($\varphi_r = 45.86°$) by requiring the z_r-axis to be parallel to the wave vector of the perturbed mode resulting from the PLST computations at $x = 3.32$ ($x_r \approx 2.61$, dashed line in the figure). At the position considered, the vortex axes are indeed parallel to the x_r-axis. We will make use of this in the following in order to choose the orientation of the vortex-oriented coordinate system for the SLST computations.

Some relevant flow quantities over the crosscut plane $x_r = 2.61$ of figure 4 are shown in figure 5. The plane is orthogonal to the vortex axes and covers approximately one fundamental spanwise wavelength of the dominating mode (0, 1). The observer looks in the downstream direction. Figures 5(*b*), 5(*e*) and 5(*f*) allow a clear identification of the vortical motion, while figures 5(*a*), 5(*c*) and 5(*d*) visualize its effect on the streamwise velocity $\tilde{u}_r$ and on its gradients over y and z_r, i.e. on quantities which are known to be relevant for the secondary instability of the flow. All quantities show the typical distribution for CF-dominated boundary layers with large-amplitude steady vortices (cf. Lerche 1997; Wassermann & Kloker 2002).

4.1.2. *Unsteady fundamental case*

The large-amplitude primary travelling vortices of the unsteady fundamental case are visualized in figure 6. No lateral counter-rotating vortices are visible which is different from the steady case and, as a consequence of the dependence of the propagation direction of CF modes on their frequency, the direction of the vortex axes is different from that in the steady case. The orientation of the reference system for the visualization ($\varphi_{m,r} = 37.77°$) has been defined with the $z_{m,r}$-axis parallel to the wave vector of mode (1, 1) at $x = 3.32$ ($x_{m,r} \approx 2.30$, dashed line in the figure). Also in this case, perfect matching is observed between the direction of the vortex axes and

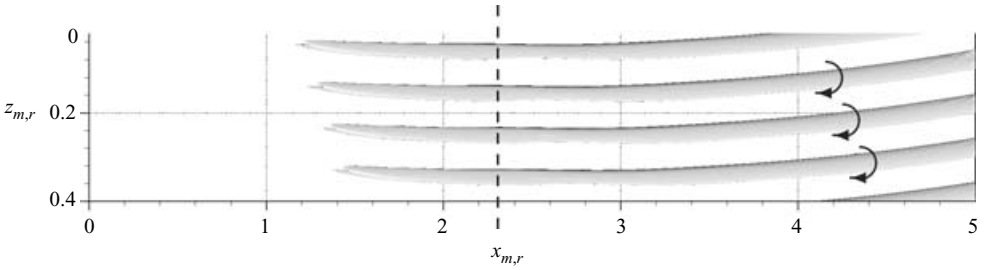

FIGURE 6. Visualization of vortical structures (λ_2-isosurfaces, $\lambda_2 = -5$) for the unsteady fundamental case ($x_{0,m,r} = 1.5$, $z_{0,m,r} = 0.07$, $\varphi_{m,r} = 37.77°$). Arrows indicate the rotation directions of the vortices. The dashed line shows the position of the crosscut plane of figure 7.

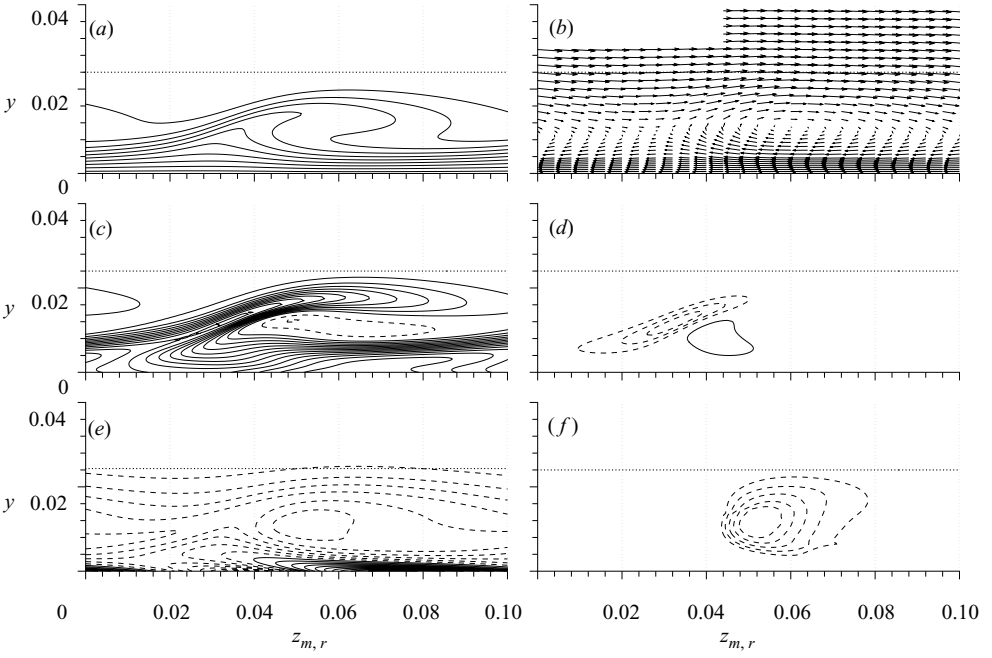

FIGURE 7. The flow field in the crosscut plane $x_{m,r} = 2.30$ of figure 6 ($x \approx 3.32$): (*a*) $\tilde{u}_{m,r}$-isocontours, $\Delta = 0.1$; (*b*) $[\tilde{w}_{m,r}, \tilde{v}_{m,r}]$-vectors; (*c*) $\partial\tilde{u}_{m,r}/\partial y$-isocontours, $\Delta = 10.0$; (*d*) $(\partial u_{m,r}/\partial z_{m,r})/u_{b,s,e}$-isocontours, $\Delta = 10.0$; (*e*) $\tilde{\omega}_{x,m,r}$-isocontours, $\Delta = 2.5$; (*f*) λ_2-isocontours, $\Delta = 5.0$. The reference system (x_m, y, z_m) moves in the spanwise direction with velocity c_m equal to the phase velocity of the perturbed primary mode. Velocities are computed with respect to the moving frame: $u_m = u$, $w_m = w - c_m$. Dashed lines correspond to negative values. The horizontal dotted line denotes the undisturbed boundary-layer thickness.

that of the wavefronts of the generating instability. In the moving system considered in figure 6, the flow is steady and the vortices are fixed.

General analogy and some differences with respect to the steady case are found in figure 7 for the flow quantities in the crosscut plane $x_{m,r} = 2.30$ of figure 6 (notice that the reference system is moving and also velocities are computed with respect to the moving observer). Again a water-wave shape is visible in the $\tilde{u}_{m,r}$-profiles, but in comparison to the steady case it is compressed in the wall-normal direction and stretched in the spanwise direction (figure 7*a*). The vortex is closer to the wall

(figure 7*b* and 7*f*), wall-normal gradients are larger (figure 7*c*) and spanwise ones are lower (figure 7*d*), as already observed by Wassermann & Kloker (2003). Within the vortex core, the vorticity component $\tilde{\omega}_{x,m,r}$ is larger in absolute value, whereas on its updraft side the region of positive vorticity vanishes completely. This complies with the absence of a lateral counter-rotating vortex at that position.

4.2. *Definition of the primary state for SLST computations*

It is common practice to extract the simplified primary state for SLST computations from available descriptions of the flow provided by PSE or DNS (e.g. Malik & Chang 1994; Janke & Balakumar 2000; Messing 2004). However, some open questions remain, since the basic assumptions of the SLST are not sufficient to determine the extraction procedure uniquely. For our computations, we defined the primary state on the basis of the DNS flow fields documented in § 4.1 and considered three different extraction procedures, all of which fulfil the basic SLST assumptions. Details of the primary-state definition are presented hereinafter only for the fundamental steady case, but the unsteady fundamental case is completely analogous.

Indicating by $x = x_{SLST}$ the position at which the SLST analysis is carried out, we follow the results from the previous section and define the vortex-oriented reference system (angle φ_v) by requiring the z_v-axis to be parallel to the wave vector of the perturbed primary mode resulting from PLST computations. We indicate by $[\breve{u}_v\ \breve{v}_v\ \breve{w}_v]^T(y, z)$ the velocity components of the DNS flow field with reference to the (x_v, y, z_v)-axes, restricted to $x = x_{SLST}$, and expressed as functions of the remaining plate-oriented coordinates. We then define $\gamma_{0,v} = \gamma_0/\cos(\varphi_v)$ and consider the Fourier expansions

$$[\breve{u}_v\ \breve{v}_v\ \breve{w}_v]^T(y, z) = \sum_{k=-\infty}^{+\infty} \left[\hat{\breve{u}}_{v,(k)}\ \hat{\breve{v}}_{v,(k)}\ \hat{\breve{w}}_{v,(k)}\right]^T(y) \exp(\mathrm{i}k\gamma_0 z), \tag{4.1}$$

$$[\dot{u}_v\ \dot{v}_v\ \dot{w}_v]^T(y, z_v) = \sum_{k=-\infty}^{+\infty} \left[\hat{\dot{u}}_{v,(k)}\ \hat{\dot{v}}_{v,(k)}\ \hat{\dot{w}}_{v,(k)}\right]^T(y) \exp(\mathrm{i}k\gamma_{0,v} z_v), \tag{4.2}$$

for the restricted DNS flow and for the SLST primary state in the respective directions of periodicity.

Differences between various extraction procedures originate because, since the primary state is assumed to be constant in x_v-direction, the continuity equation reduces to

$$\frac{\partial \hat{\dot{v}}_{v,(k)}}{\partial y} + \mathrm{i}k\gamma_{0,v}\, \hat{\dot{w}}_{v,(k)} = 0, \qquad \forall k, \tag{4.3}$$

and connects the velocity components $\dot{v}_v$ and $\dot{w}_v$. As a consequence, if continuity has to be granted, $\dot{v}_v$ and $\dot{w}_v$ may not be defined independently by extracting both of them from the DNS flow field. However, it is not evident which component should be extracted from the DNS and which, on the contrary, should be determined through (4.3). An option is, of course, also to extract both components from the DNS flow field and violate the continuity equation.

We consider the following alternative definitions for the primary state:

v_v-fixed approach

$$\hat{\dot{u}}_{v,(k)}(x_v, y) = \hat{\breve{u}}_{v,(k)}(y), \qquad \forall k, \forall x_v, y, \tag{4.4a}$$

$$\hat{\dot{v}}_{v,(k)}(x_v, y) = 0, \qquad k = 0, \forall x_v, y, \tag{4.4b}$$

$$\hat{\dot{v}}_{v,(k)}(x_v, y) = \hat{\breve{v}}_{v,(k)}(y), \qquad k \neq 0, \forall x_v, y, \tag{4.4c}$$

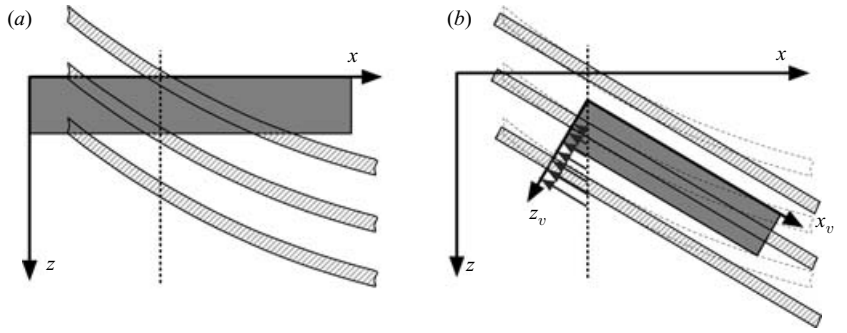

FIGURE 8. Reference systems, integration domains (grey) and schematic representation of the primary vortices (hatched) for (*a*) the original DNS, and (*b*) for the SLST primary state. Dashed lines represent the plane $x = x_{SLST}$. Arrows in (*b*) connect points with identical velocity vectors in the planes $x = x_{SLST}$ and $x_v = 0$.

$$\hat{\dot{w}}_{v,(k)}(x_v, y) = \hat{\mathring{w}}_{v,(k)}(y), \qquad k = 0, \forall x_v, y, \tag{4.4d}$$

$$\hat{\dot{w}}_{v,(k)}(x_v, y) = \frac{\mathrm{i}}{k\gamma_{0,v}} \frac{\mathrm{d}\hat{\mathring{v}}_{v,(k)}}{\mathrm{d}y}(y), \qquad k \neq 0, \forall x_v, y, \tag{4.4e}$$

w_v-fixed approach

$$\hat{\dot{u}}_{v,(k)}(x_v, y) = \hat{\mathring{u}}_{v,(k)}(y), \qquad \forall k, \forall x_v, y, \tag{4.5a}$$

$$\hat{\dot{v}}_{v,(k)}(x_v, y) = \int_0^y -\mathrm{i}k\gamma_0 \hat{\dot{w}}_{v,(k)}(\eta)\,\mathrm{d}\eta, \qquad \forall k, \forall x_v, y, \tag{4.5b}$$

$$\hat{\dot{w}}_{v(k)}(x_v, y) = \hat{\mathring{w}}_{v,(k)}(y), \qquad \forall k, \forall x_v, y, \tag{4.5c}$$

v_v-w_v-fixed approach

$$\hat{\dot{u}}_{v,(k)}(x_v, y) = \hat{\mathring{u}}_{v,(k)}(y), \qquad \forall k, \forall x_v, y, \tag{4.6a}$$

$$\hat{\dot{v}}_{v,(k)}(x_v, y) = \hat{\mathring{v}}_{v,(k)}(y), \qquad \forall k, \forall x_v, y, \tag{4.6b}$$

$$\hat{\dot{w}}_{v(k)}(x_v, y) = \hat{\mathring{w}}_{v,(k)}(y), \qquad \forall k, \forall x_v, y. \tag{4.6c}$$

In the v_v-fixed approach, the wall-normal component $\dot{v}_v$ is extracted from the DNS flow field (equation (4.4*c*)) and $\dot{w}_v$ follows from the continuity equation (equation (4.4*e*)). In the w_v-fixed approach, $\dot{w}_v$ is defined on the basis of the DNS data (equation (4.5*c*)) and $\dot{v}_v$ is computed integrating the continuity equation in the y-direction and imposing the no-slip condition at the wall (equation (4.5*b*)). In the v_v-w_v-fixed approach, both velocity components are set equal to the corresponding components from the DNS (equations (4.6*b*) and (4.6*c*)) and the continuity equation is not fulfilled. In all cases, the velocity component $\dot{u}_v$, which does not appear in the continuity equation, is defined according to the DNS flow field (equations (4.4*a*), (4.5*a*) and (4.6*a*)). Finally, for the spanwise constant harmonic $k = 0$, the continuity equation requires $\dot{v}_{v,(0)}$ to be identically zero and poses no constraint on $\dot{w}_{v,(0)}$, which explains the use of (4.4*b*) and (4.4*d*) in the v_v-fixed approach. For all approaches, the vorticity field is computed as a final step, consistent with the velocity field delivered by the extraction procedure.

Figure 8 is a conceptual sketch of the relation between the original DNS flow and the resulting SLST primary state. According to the v_v-w_v-fixed approach, the primary

state is defined at each point by shifting in the x_v-direction the restriction of the DNS flow field to the plane $x = x_{SLST}$. As a consequence, the vortex axes in figure 8(*b*) are straight and the periodicity length in the z_v-direction is shorter than the original periodicity length in the z-direction. Differences in the velocity components are less than 0.5% of the local free-stream velocity. Larger and smaller flow structures appear to be identical in all cases on visual inspection.

Since the continuity equation and the definition of the vorticity vector are implicitly assumed in the formulation of the SLST solver for both primary state and perturbation, primary states defined according to the v_v-w_v-fixed approach may not be handled with the available SLST code. Results for that approach have been obtained only by means of the linearized DNS code with spanwise periodic base flow.

Malik & Chang (1994) and Janke & Balakumar (2000), who estimated the primary state by means of PSE computations, do not provide a detailed description of the procedure used to define the SLST primary state. Malik & Chang (1994) mention, however, that dropping the wall-normal velocity of the primary state significantly increases secondary amplification rates. Messing (2004) adopted the v_v-fixed approach. Koch *et al.* (2000) obtained the SLST primary state from equilibrium solutions of the primary perturbations, which are already constant in the x_v-direction and also fulfil the continuity equation. They merely took the equilibrium solutions as they were and did not need an extraction procedure.

5. Comparison of SLST and DNS

5.1. *The steady fundamental case*

Direct numerical simulations have been carried out introducing low-amplitude background pulsing within the saturation region of the steady fundamental case documented in § 4.1. Unsteady harmonic waves with $\omega = h\omega_0$, $h = 1, \ldots, 50$, $\gamma = \pm\gamma_0$ ($\omega_0 = 6$ and $\gamma_0 = 52.4$) were perturbed at $x = 3$ in the DNS case *Steady+Pulse*. Restricting the secondary forcing to the first spanwise harmonic $\gamma = \pm\gamma_0$ was not a limiting factor, since unsteady modes with higher spanwise wavenumbers could be readily generated by nonlinear interaction of the perturbed modes with the high-amplitude primary perturbation. Also, the relative phase of the perturbed waves could be chosen arbitrarily since no interaction can be expected between secondary perturbations with different frequencies, as far as linearity in the sense of the SLST is ensured. Discretization parameters were identical to those for the simulations of the primary state ($\Delta x = 0.1309 \times 10^{-2}$ and $\Delta y_{min} = 0.1147 \times 10^{-3}$, $\gamma_{max} = 13\gamma_0$, $\Delta t = 3.49 \times 10^{-4}$).

The growth of secondary modes downstream of $x = 3.0$ becomes evident in figure 9, where t-modal amplitudes of the streamwise velocity components $\tilde{u}'_s$ (maximum values over y and z) are plotted as functions of the x-coordinate. The maximal growth rates are achieved by high-frequency modes ($\omega \approx 120$). In spite of lower initial amplitudes, which are due to a decrease in the receptivity for increasing frequency, curves for $\omega \approx 120$ soon rise over those associated with lower frequencies. The delayed explosive growth of modes $\omega > 180$ for $x > 3.5$ is nonlinearly induced by the leading modes $\omega \approx 120$.

The SLST analysis has been carried out at the downstream position $x_{SLST} = 3.32$, for which the primary state has been documented in § 4.1. Figure 9 shows that at that position, near-field effects connected to the secondary forcing at $x = 3$ have already died out and secondary perturbations are still small enough to ensure linear behaviour (modal amplitudes lower than 0.01%). The vortex-oriented system was defined by

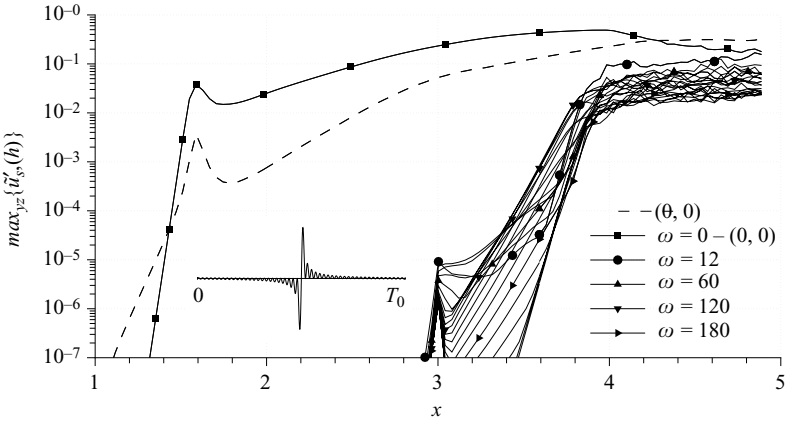

FIGURE 9. Downstream development of the modal amplitudes $\tilde{u}'_{s,(h)}$ from Fourier expansion in time (maximum over y and z, $0 \leqslant \omega \leqslant 240$, $\Delta\omega = 12$) for case *Steady+Pulse*. The inset shows the time signal of the pulsing in physical space.

setting $\varphi_v = 45.86°$ in agreement with the results of § 4.1. The v_v-fixed and the w_v-fixed approaches were considered to define the primary state. As far as numerical discretization is concerned, the Fourier expansion in the z_v-direction was truncated at the thirteenth harmonic for both primary state and secondary perturbation as in the DNS. The step size in the wall-normal direction was $\Delta y = 0.6593 \times 10^{-3}$ and the upper edge of the integration domain was located at $y_e = 0.053$.

Post-processing of the DNS results presented hereinafter refers to the rotated reference system with origin in $x_{0,r} = x_{SLST} = 3.32$ and oriented as the vortex-oriented reference system of the SLST: $\varphi_r = \varphi_v = 45.86°$.

5.1.1. *Wavenumbers and amplification rates*

Spatial amplification rates $\mathrm{Im}(\alpha_r)$ and wavenumbers $\mathrm{Re}(\alpha_r)$ in x_r-direction for the unsteady harmonic components of the DNS flow field have been evaluated in analogy with the SLST ansatz. (The subscript r indicates the reference system to which the complex wavenumber α_r refers. We do not use the subscripts r and i to indicate real and imaginary part of a complex number.) We considered Fourier coefficients $\hat{u}'_{r,(h)}$ of the velocity component u'_r parallel to the main vortex axis and, in analogy with (2.3), computed $\alpha_r = \mathrm{Re}(\alpha_r) + \mathrm{i}\mathrm{Im}(\alpha_r)$ by setting

$$\alpha_r = -\mathrm{i}\left.\frac{\partial \ln \hat{u}'_{r,(h)}}{\partial x_r}\right|_{x_r=0,\, y=y_{max},\, z_v=z_{v,max}}, \tag{5.1}$$

where $(y_{max}, z_{v,max})$ is the position in the plane $x_r = 0$ at which $|\hat{u}'_{r,(h)}|_{x_r=0}$ achieves its maximum. The resulting values for $\mathrm{Im}(\alpha_r)$ and $\mathrm{Re}(\alpha_r)$ are compared in figure 10 to the corresponding quantities for spatially developing modes from the SLST (cf. (2.4*a*)) for different definitions of the primary state. Results are reported only for the most unstable modes of each type.

Perturbations developing in the DNS may be identified as type III modes in the low-frequency range ($\omega < 60$) and as type I modes for higher frequencies. The divergence of the DNS amplification rates for $\omega > 220$ is due to nonlinear generation of those modes through the leading ones ($\omega \approx 120$). However, the agreement between theory and DNS is not unequivocal. On the one hand, amplification rates from the DNS

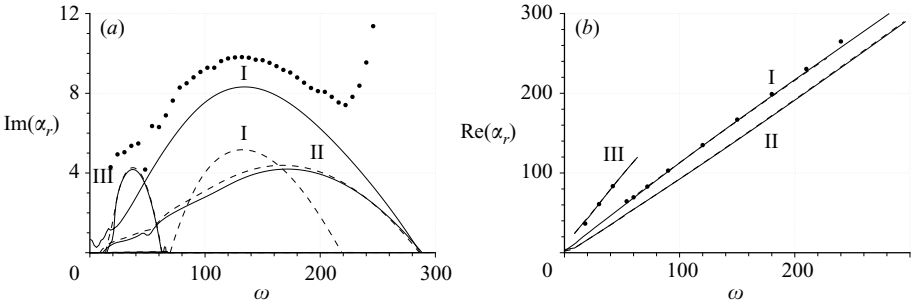

FIGURE 10. (*a*) Spatial amplification rates and (*b*) wavenumbers in the $x_r = x_v$ direction ($\varphi_r = \varphi_v = 45.86°$) from SLST according to the w_v-fixed approach (solid lines), and the v_v-fixed approach (dashed lines), and from DNS (dots) as functions of the frequency for unstable secondary modes.

are significantly larger than those from the theory (figure 10*a*), which moreover for the type I mode strongly depend on the approach considered for the definition of the primary state. On the other hand, a perfect matching is found for the wavenumbers (figure 10*b*), independent of the approach.

We would expect the most unstable modes according to the SLST to develop in the DNS. This is indeed the case if DNS results are compared to amplification rates from the SLST for the w_v-fixed approach. In the former, no type II modes are observed, and in the latter, type I modes achieve, for any frequency, larger amplification rates than type II modes. On the contrary, disagreement is given between DNS and the v_v-fixed apprach, according to which type II modes are more strongly amplified than type I modes for $\omega > 170$. Evidently, the determination of the most amplified mode is not unequivocal within the margin of uncertainty connected to the definition of the primary state in SLST. In the light of these results it seems reasonable to explain the discrepancies observed by different authors with respect to the relative amplification rates of type I and type II modes as a consequence of the inaccuracy in the SLST results.

The dispersion relations in figure 10(*b*) are approximated well by straight lines through the origin so that all modes of a given type are characterized by similar values of the phase and group velocities ($c_{ph,v}$ and $c_{gr,v}$, respectively), independently of their frequencies. In general, type I ($c_{ph,r} \approx 0.9$) and type II modes ($c_{ph,r} \approx 1.1$) are faster than type III modes ($c_{ph,r} \approx 0.5$). Similar values have been found by Koch *et al.* (2000).

5.1.2. *Amplitude distribution*

In accordance with the SLST ansatz (cf. (2.3)), normalized amplitude distributions over the plane $x_r = 0$ for the unsteady harmonics $\hat{u}'_{r,(h)}$, $h > 0$, of the DNS flow field, are compared in figure 11 to the corresponding component $\ddot{u}_v$ of SLST eigenfunctions for the same frequency (see also (2.4*a*)). Data refer to the most amplified modes of each type. All displayed SLST eigenfunctions have been obtained by defining the primary state according to the w_v-fixed approach; however, eigenfunctions resulting from the v_v-approach have been found to be nearly identical.

The eigenfunction shapes confirm the identification of the dominating instability as a type III mode at moderate frequencies ($\omega = 36$, figure 11*b*) and as a type I mode at higher frequencies ($\omega = 120$, figure 11*a*). The agreement between DNS and SLST is nearly perfect in both cases. The slight downward shift of the DNS amplitudes

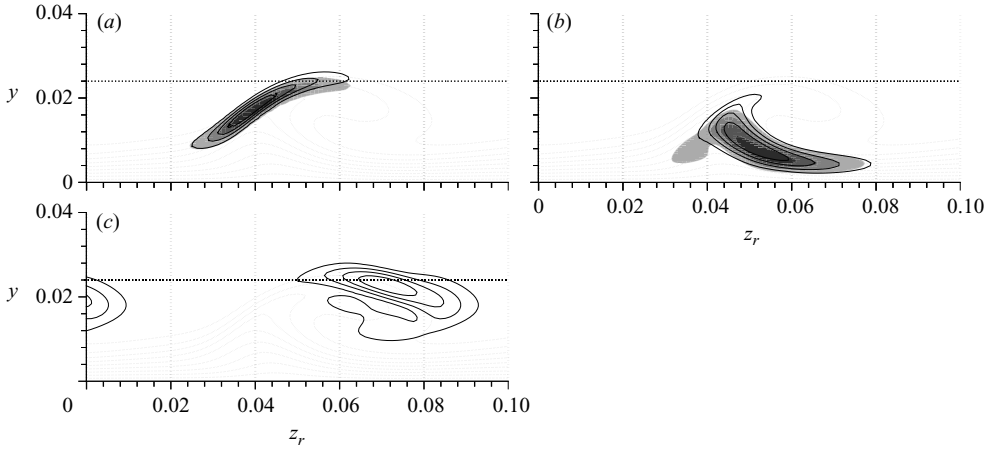

FIGURE 11. Normalized $\ddot{u}_r$-amplitude distributions for unstable secondary modes from SLST (lines, $\Delta = 0.2$) and DNS (shaded, $\Delta = 0.2$) in a plane normal to the primary-vortex axis ($\varphi_r = \varphi_v = 45.86°$). The primary state for the SLST has been extracted according to the w_v-fixed approach. The horizontal dotted line denotes the undisturbed boundary-layer thickness. (*a*) Type I: $\mathrm{Re}(\alpha_r) \approx 146$, $\omega \approx 132$; (*b*) Type III: $\mathrm{Re}(\alpha_r) \approx 72$, $\omega \approx 36$; (*c*) Type II: $\mathrm{Re}(\alpha_r) \approx 162$, $\omega \approx 170$.

may be justified considering that in the DNS, perturbations develop along the x-direction and, before reaching the plane considered for the visualization, cross regions characterized by lower boundary-layer thicknesses. Amplitude distributions similar to those associated with type II modes (figure 11*c*) were not observed for any frequency in the DNS.

5.2. *Unsteady fundamental case*

Validation of the secondary stability theory for the unsteady fundamental case has been achieved on the basis of the unsteady primary state described in § 4.1. Post-processing of the DNS flow field and SLST computations were thereby carried out referring to the system (x_m, y, z_m) translating in the z-direction with the phase velocity $c_m = \omega_0/\gamma_0$ of the primary perturbation (see § 2.1).

Analogously to § 5.1, secondary modes have been triggered in the DNS case *Unsteady+Pulse* at $x = x_m = 3$ by perturbing low-amplitude harmonic waves with $\omega_m = h_m\omega_0$, $h_m = 1, \ldots, 50$, and $\gamma_m = \pm\gamma_0$ ($\omega_0 = 6$, $\gamma_0 = 52.4$). (When defining the secondary perturbation, reference is made to modal components from Fourier expansions in the moving system. Frequencies and wavenumbers from expansions in the fixed system would be $(h, k) = (h_m + k_m, k_m)$, see Wassermann & Kloker 2003). The SLST analysis has been carried out extracting the primary state from the plane $x_{SLST,m} = 3.32$ and the vortex-oriented reference system was defined setting $\varphi_{v,m} = 37.77°$. Discretization parameters for both DNS and SLST were identical to those in § 5.1.

Figure 12 shows the amplitude development of the t-modal components $\tilde{u}'_{m,s,(h)}$. Since the Fourier expansion is computed in the moving system, the frequency $\omega_m = 0$ corresponds to the primary perturbation, which is steady in that system. Similarly to the steady fundamental case, frequencies $\omega_m \approx 120$ undergo the strongest amplification and dominate in spite of the fact that, owing to receptivity effects, their amplitudes are initially lower than those of low-frequency modes. The position $x_{SLST,m} = 3.32$

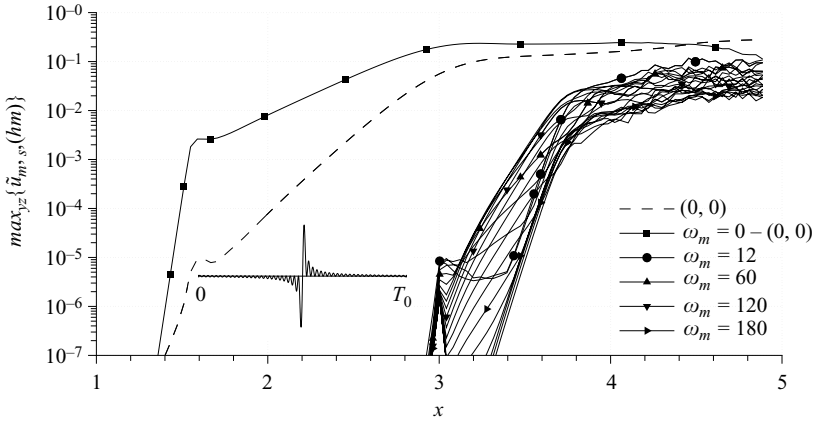

FIGURE 12. Downstream development of the modal amplitudes $\tilde{u}'_{m,s,(h_m)}$ from Fourier expansion in time (maximum over y and z, $0 \leqslant \omega_m \leqslant 240$, $\Delta\omega_m = 12$) for case *Unsteady+Pulse*. The inset shows the time signal of the pulsing in physical space.

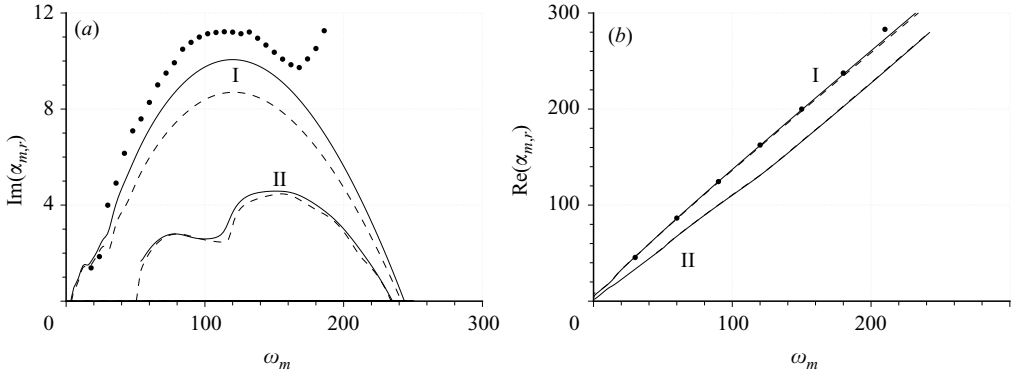

FIGURE 13. (*a*) Spatial amplification rates and (*b*) wavenumbers in the $x_{m,r} = x_{m,v}$ direction ($\varphi_{m,r} = \varphi_{m,v} = 37.77°$) from SLST according to the w_v-fixed approach (solid lines), and the v_v-fixed approach (dashed lines), and from DNS (dots) as functions of the frequency for unstable secondary modes.

chosen for the comparison of DNS and SLST lies in a region where exponential growth is well established for secondary modes and amplitudes are still small.

Post-processing of the DNS results has been carried out referring to the rotated moving reference systems $(x_{r,m}, y, z_{r,m})$ with origin in $x_{r,m,0} = x_{SLST}$. Fourier modal components are computed for flow quantities expressed as functions of the coordinates of the moving systems.

5.2.1. *Wavenumber and amplification rates*

Amplification rates and streamwise wavenumbers for secondary modes from DNS and SLST are plotted in figure 13. Amplification rates from the DNS are evaluated on the basis of the spatial development of the modal amplitudes $u'_{m,r,(h)}$ in the $x_{m,r}$-direction, analogously to (5.1). Perturbations developing in the DNS are clearly found to be type I modes, but also in this case agreement between DNS and SLST is quantitatively not unequivocal. Although the dispersion relations match nearly perfectly, discrepancies are found with respect to the amplification rates. Differences

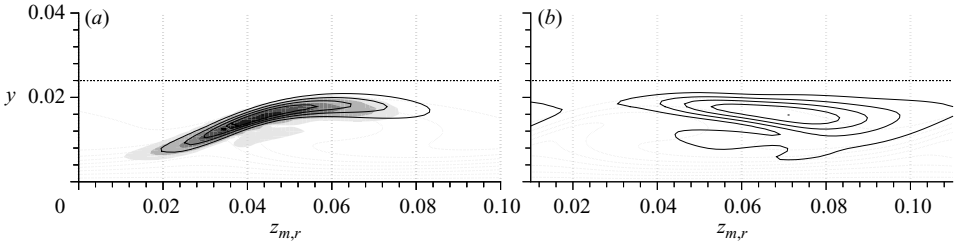

FIGURE 14. Normalized $\ddot{u}_{m,r}$-amplitude distributions for unstable secondary modes from SLST (lines, $\Delta = 0.2$) and DNS (shaded, $\Delta = 0.2$) in a plane normal to the primary-vortex axis ($\varphi_{m,r} = \varphi_{m,v} = 37.77°$). The primary state for the SLST has been extracted according to the w_v-fixed approach. The horizontal dotted line denotes the undisturbed boundary-layer thickness. (*a*) Type I: $\mathrm{Re}(\alpha_{m,r}) \approx 162$, $\omega_m \approx 120$; (*b*) Type II: $\mathrm{Re}(\alpha_{m,r}) \approx 174$, $\omega_m \approx 156$.

between DNS and SLST, and the sensitivity of the latter on the approach used for the definition of the primary state are smaller than in the steady fundamental case.

Type I modes are the most amplified instabilities for all frequencies and no unstable type III mode is found. Again, phase and group velocities are almost constant for given modes and slightly lower than in the steady case, being $c_{ph,m,r} \approx 0.7$ for type I modes and $c_{ph,m,r} \approx 0.9$ for type II modes. This is only partially because $c_{ph,m,r}$ is computed here with respect to the moving reference system (x_m, y, z_m) which moves with respect to the fixed system (x, y, z) with a positive velocity component $c_{m,r}$ in the $x_{m,r}$-direction ($c_{m,r} = c_m \sin\varphi_{m,r} = \omega_0/\gamma_0 \sin\varphi_{m,r} = 0.070$).

5.2.2. *Amplitude distributions*

Normalized amplitude distributions from DNS and SLST are compared in figure 14. DNS results refer to amplitudes from a Fourier expansion in time of the perturbation velocity $u'_{m,r}$ (modal components $\hat{u}'_{m,r,(h)}$, $h > 0$). Eigenfunctions $\ddot{u}_{v,m}$ from the SLST have been obtained defining the primary state according to the w_v-fixed approach and refer to the type I and type II modes already discussed in the previous section. Apart from the slight downward shift of the DNS eigenfunctions already observed in the steady case, the agreement between DNS and SLST with respect to the type I mode is nearly perfect. Since the amplification rates of type II modes are lower than those of type I modes, the former could not be observed in the DNS.

6. Origin of the inexactness of SLST amplification rates

We investigated the origin of the deviations observed in § 5 between amplification rates from DNS and SLST. First of all, errors in the numerical procedures were ruled out showing that both the DNS and the SLST provide identical results when the flow field of the former reproduces the simplified configuration of the latter. In a second step, the influence of different simplifying assumptions in the definition of the SLST problem has been investigated. Only results for cases with steady primary perturbations are presented, but there is little doubt that analogous results hold also in the unsteady case.

The linearized code with three-dimensional spanwise-periodic base flow has been used for all DNS presented in this section. In all cases, the base flow was set equal to the primary state of the SLST, which was possible since the perturbation formulation of the DNS does not require the base flow to be a solution of the Navier–Stokes

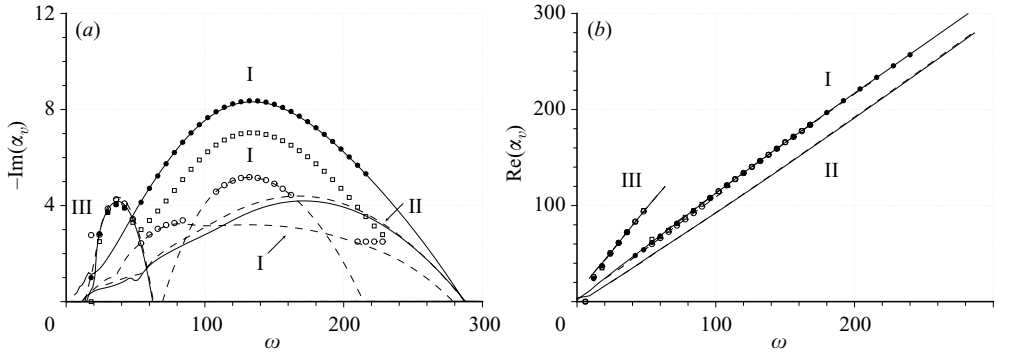

FIGURE 15. (*a*) Spatial amplification rates and (*b*) wavenumbers in the $\breve{x} = x_v$ direction ($\breve{\varphi} = \varphi_v = 45.86°$) from SLST (lines) and from adapted DNS (case *Adapted-vortex-oriented*, symbols) as functions of the frequency. The primary states for the SLST and the three-dimensional base flows for the DNS have been defined according to the w_v-fixed approach (solid lines, dots), the v_v-fixed approach (dashed lines, circles) and to the v_v-w_v-fixed approach (only DNS, squares).

equations, exactly as in the SLST. All results have been obtained for primary states corresponding to the steady fundamental case of § 4.1 at $x_{SLST} = 3.32$.

Discretization parameters for DNS and SLST were identical to those of § 5 with the exception of the wall-normal discretization for the DNS. Since the primary vortex with its discretization-critical near-wall region was included in the base flow, the step size in the wall-next block could be doubled ($\Delta y_{min} = 0.2295 \times 10^{-3}$) and the time step could be correspondingly increased ($\Delta t = 6.54 \times 10^{-4}$). Finally, since the primary state was invariant in the streamwise direction, the position at which secondary perturbations were initiated is not significant, as long as undue interactions with inlet or outflow boundaries are prevented. In agreement with § 5, results are presented referring to the vortex-oriented reference system ($\varphi_r = \varphi_v = 45.86°$).

6.1. *Comparison of SLST and adapted DNS*

The base flow for the DNS case *Adapted-vortex-oriented* reproduced exactly the primary state for the SLST computation. The reference system $(\breve{x}, y, \breve{z})$ for the DNS was rotated with respect to the standard plate-oriented system and identical to the vortex-oriented system considered for the SLST computations ($\breve{\varphi} = \varphi_v = 45.86°$, see figure 18). The spanwise periodic base flow $[\breve{u}_b, \breve{v}_b, \breve{w}_b]^T(\breve{x}, y, \breve{z})$ was defined according to the v_v-fixed, the w_v-fixed and the v_v-w_v-fixed approaches. The actual definition followed (4.4), (4.5) and (4.6) after substitution of $\dot{u}$ with $\breve{u}_b$, x_v with $\breve{x}$ and so on. SLST computations were carried out for both the v_v-fixed and the w_v-fixed approaches.

Results for the adapted DNS and for the corresponding SLST computations are presented in figure 15. The agreement is perfect, both for the v_v-fixed and the w_v-fixed approaches. Amplification rates for the v_v-w_v-fixed approach, which cannot be computed within the wall-normal-velocity–wall-normal-vorticity formulation of the SLST code, are intermediate between those for the v_v-fixed and the w_v-fixed approaches. Streamwise wavenumbers collapse for all approaches. As we may expect from the good agreement between SLST and standard DNS in figure 11, the agreement of SLST and adapted DNS with respect to the amplitude distributions is perfect and is not shown.

Figure 15 rules out inaccuracies of the numerical solutions or of the Gaster transformation, (2.4), used to convert temporal SLST amplification rates into spatial ones (see also Koch *et al.* (2000) for a validation of the Gaster transformation) as

possible causes for the deviations between non-adapted DNS and SLST. Errors in the SLST evaluation of the amplification rates may only be attributed to the simplified representation of the primary state.

6.2. *Influence of the periodicity and spatial-amplification direction*

Differences in the choice of the directions of exponential growth and periodicity for the secondary perturbation might be causes of discrepancy between DNS and SLST. In this section, we show that this is not the case. Periodicity is indeed neither an intrinsic nor a necessary characteristic of the instability. As a collateral result, we show that the investigation of detuned modes is futile when considering crossflow-induced secondary instabilities since results for the tuned problems are already exhaustive. Both results are trivial conclusions if it can be shown that each single maximum in the periodic eigenfunctions of the tuned problems (see figure 11) actually represents an independent eigenfunction of the stability problem, developing independently from neighbouring maxima and interacting only with the primary vortex next to it. After reviewing results from the literature, we turn to the verification of this statement and then derive the implications we started from.

Koch *et al.* (2000) carried out spatial SLST computations assuming exponential amplification in chord direction (x) and periodicity in spanwise direction (z), and showed that the resulting amplification rates were equal to those obtained by converting temporal ones by means of a generalized Gaster transformation. Starting from the consideration that in a temporal analysis no spatial amplification is given and that the flow is periodic in all wall-parallel directions, we observe that the Gaster transformation used by Koch *et al.* (2000) to compute spatial amplification rates $\mathrm{Im}(\alpha_S)$ in the x-direction is equivalent to that given in (2.4) for modes growing exponentially in the x_v-direction, but rescaled in order to take account of the stretching factor $\partial x_v/\partial x = 1/\cos\varphi_v$:

$$\mathrm{Im}(\alpha_S) = \frac{\partial \ln|\hat{\hat{u}}_{(h)}|}{\partial x} = \frac{\partial \ln|\hat{\hat{u}}_{(h)}|}{\partial x_v}\frac{\partial x_v}{\partial x} = \mathrm{Im}(\alpha_{v,S})\frac{1}{\cos\varphi_v}, \tag{6.1}$$

where $\mathrm{Im}(\alpha_S)$ and $\mathrm{Im}(\alpha_{v,S})$ are the spatial amplification rates in the x and x_v-directions, respectively. A similar transformation would hold if the perturbation growth was indeed in the x_v-direction and the fact that results obtained this way were confirmed by spatial computations, where amplification was imposed in the x-direction, is a first hint that the choice of the exponential-growth and periodicity directions might be irrelevant for the development of secondary instabilities.

The reciprocal independence of secondary-perturbation maxima may be deduced from figures 16 and 17, where results from figure 10 (case *Single-*$\lambda_{0,v}$) are compared to results from an SLST analysis considering a primary state with doubled fundamental wavelength in the z_v-direction (case *Double-*$\lambda_{0,v}$, the number of harmonics for discretization of the z_v-direction has been correspondingly doubled). One wavelength of case *Double-*$\lambda_{0,v}$ contains two primary vortices, where one has been manipulated by suppressing its perturbation over a limited z_v-interval. The velocity field has been multiplied by the function $[1 - h(z_v)]$, where $h(z_v)$ is a Hanning window stretching over the intervals enclosed by vertical lines in figure 16. The perturbation maximum at the side of the unmodified right-hand vortex is still an eigensolution of the stability problem with nearly identical eigenvalue, even if the maximum next to the modified left-hand vortex has been completely suppressed. More exactly, the eigenfunction associated to the manipulated vortex has been modified shifting its eigenvalue, so

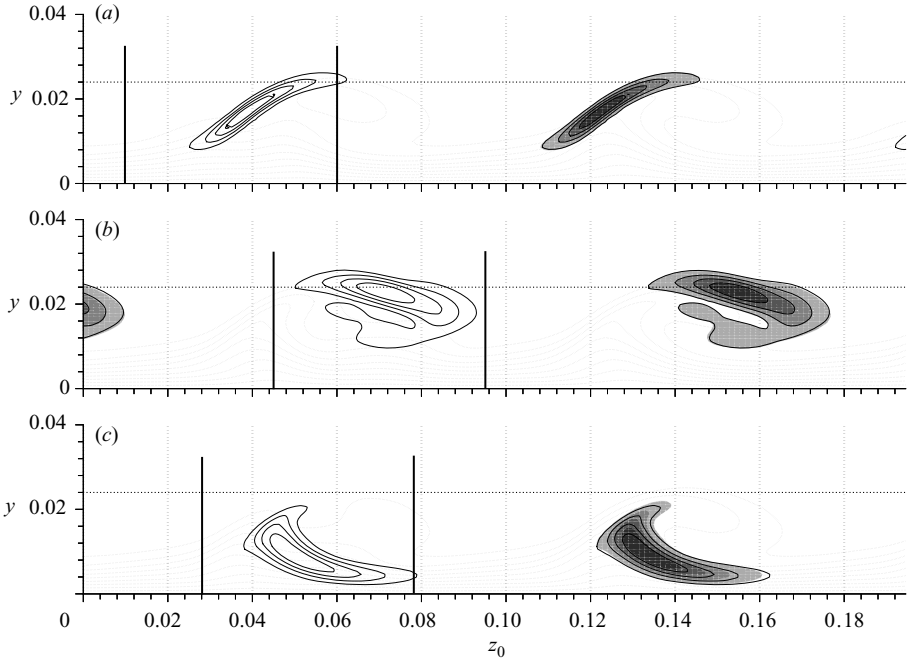

FIGURE 16. Normalized $\ddot{u}_v$-amplitude distributions for secondary modes from SLST computations for case *Single*-$\lambda_{0,v}$ (lines, $\Delta = 0.2$) and case *Double*-$\lambda_{0,v}$ (shaded without lines, $\Delta = 0.2$) in a plane normal to the primary-vortex axis ($\varphi_v = 45.86°$). The primary state for the SLST has been extracted according to the w_v-fixed approach and manipulated for case *Double*-$\lambda_{0,v}$ in the regions enclosed by vertical lines. The horizontal dotted line denotes the undisturbed boundary-layer thickness. (*a*) Type I: $\mathrm{Re}(\alpha_v) = 146$, $\omega \approx 132$; (*b*) Type II: $\mathrm{Re}(\alpha_v) = 162$, $\omega \approx 170$; (*c*) Type III: $\mathrm{Re}(\alpha_v) = 72$, $\omega \approx 36$.

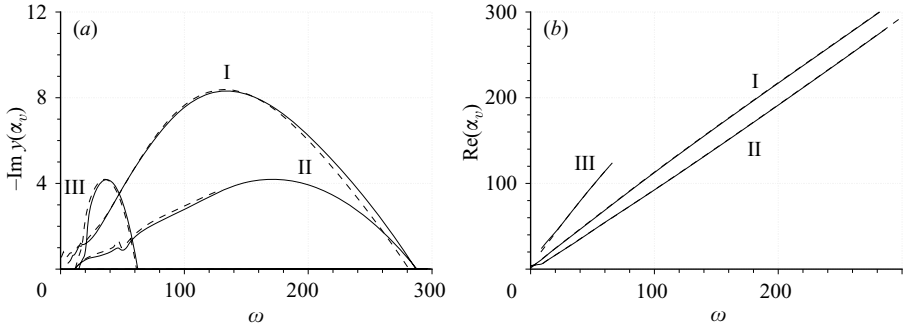

FIGURE 17. (*a*) Spatial amplification rates and (*b*) wavenumbers in the x_v-direction ($\varphi_v = 45.86°$) from SLST computations for case *Single*-$\lambda_{0,v}$ (solid lines) and case *Double*-$\lambda_{0,v}$ (dashed lines). See caption of figure 16 for details of the definition of the primary states.

that the superposition of the two eigenfunctions associated to the two neighbouring vortices is not an eigenfunction itself any more.

The moderate deviations in the amplification rates of figure 17 are probably due to the limited spanwise discretization. Indeed, the amplitude decay of higher Fourier harmonics from the spanwise discretization of the type I mode in case *Double*-$\lambda_{0,v}$ is maximal for frequencies $30 \leqslant \omega \leqslant 60$, which is also the range where the agreement

between amplification rates is nearly perfect. Moreover, owing to the non-locality of the Fourier discretization used in the z_v-direction, in the case of not fully adequate discretization, the manipulation of the primary state in a limited region is not possible without influencing the whole flow field. However, this inexactness does not affect the meaning of the present results. Indeed, there is no doubt that the single-maximum eigensolution of case *Double-*$\lambda_{0,v}$ would be an eigensolution if the primary flow had not been manipulated. This implies that the eigensolution of case *Single-*$\lambda_{0,v}$ is actually a superposition of two single-maximum eigenfunctions of case *Double-*$\lambda_{0,v}$, shifted by $\lambda_{0,v}$ with respect to each other. This is strictly true, independent of numerical inaccuracies.

There is no alternative to the conclusion that each perturbation maximum represents an independent eigenfunction and that amplitudes connected to each maximum rapidly decay in the z_v-direction. If both statements are true, we may interpret the periodic eigenfunctions of both *Single-*$\lambda_{0,v}$ and *Double-*$\lambda_{0,v}$ as superpositions of identical single-maximum eigenfunctions shifted with respect to each other by multiples of $\lambda_{v,0}$ in the z_v-direction. Indicating with

$$\ddot{f}_{loc}(t, x_v, y, z_v) = \hat{\ddot{f}}_{loc}(y, z_v) \exp(\mathrm{i}(\alpha_v x_v - \omega t)), \qquad \alpha_v \in \mathbb{C},\ \omega \in \mathbb{C}, \tag{6.2}$$

a localized single-maximum eigensolution of the temporal or spatial stability problem, the infinite sum

$$\ddot{f}_{\lambda_{0,v}}(t, x_v, y, z_v) = \sum_{k=-\infty}^{+\infty} \hat{\ddot{f}}_{loc}(y, z_v - k\lambda_{0,v}) \exp(\mathrm{i}(\alpha_v x_v - \omega t)), \tag{6.3}$$

provides a $\lambda_{v,0}$-periodic eigensolution for case *Single-*$\lambda_{0,v}$, while a $2\lambda_{v,0}$-periodic eigensolution for case *Double-*$\lambda_{0,v}$ is obtained, restricting the summation to odd or even values of the index k. Spatial decay of the single-maximum eigenfunctions must be fast enough to ensure convergence of the sum in (6.3). If, on the contrary, any of the two statements fails, no explanation can be given for the observed matching of the results from cases *Single-*$\lambda_{0,v}$ and *Double-*$\lambda_{0,v}$. We then conclude that both statements are valid.

A first verification of the rapid spatial decay of unstable eigenfunctions is provided by the near-identity of the common amplitude maxima from cases *Single-*$\lambda_{0,v}$ and *Double-*$\lambda_{0,v}$. Evidently, in case *Double-*$\lambda_{0,v}$, the summed contributions of all suppressed eigenfunctions at positions corresponding to maxima of non-suppressed eigenfunctions is negligible.

We now turn to the deduction of the implications. The independence of SLST results on the choice of the periodicity direction follows from the consideration that eigenfunctions with periodicity in any direction, except x_v, may be obtained by properly superposing independent single-maximum eigenfunctions, for the case of a periodic primary state. We may construct a periodic eigenfunction $\ddot{f}_\xi$ with arbitrary periodicity directions by setting

$$\ddot{f}_\xi(t, x_v, y, z_v) = \sum_{k=-\infty}^{+\infty} \hat{\ddot{f}}_{loc}(y, z_v - k\lambda_{0,v}) \exp(\mathrm{i}[\alpha_v(x_v - k\xi) - \omega t)]), \qquad \xi \in \mathbb{R}. \tag{6.4}$$

Clearly the single-maximum eigenfunction $\ddot{f}_{loc}$, the z_v-periodic eigenfunction $\ddot{f}_{\lambda_{0,v}}$ from (6.3), and $\ddot{f}_\xi$ are all expressions of the same instability phenomenon. Spatial amplification is in all cases in the x_v-direction.

Eigensolutions $\ddot{f}_\sigma$ for the detuned problem can be constructed analogously to $\ddot{f}_\xi$. For a given real detuning coefficient σ, we set

$$\ddot{f}_\sigma(t, x_v, y, z_v) = \exp(\mathrm{i}\sigma\gamma_{0,v}z_v)\sum_{k=-\infty}^{+\infty}\frac{\hat{\hat{f}}_{loc}(y, z_v - k\lambda_{0,v})\exp(\mathrm{i}(\alpha_v x_v - \omega t))}{\exp(\mathrm{i}\sigma\gamma_{0,v}(z_v - k\lambda_{0,v}))}$$
$$= \sum_{k=-\infty}^{+\infty}\exp(\mathrm{i}\sigma\gamma_{0,v}k\lambda_{0,v})\hat{\hat{f}}_{loc}(y, z_v - k\lambda_{0,v})(\exp(\mathrm{i}(\alpha_v x_v - \omega t))), \qquad \sigma \in \mathbb{R}, \tag{6.5}$$

where the first identity shows that $\ddot{f}_\sigma$, being the product of the detuning term and of a z_v-periodic function, fulfils the assumptions of the detuned problem, while the second identity proves that it is also an eigensolution of the stability problem, resulting from the superposition of eigenfunctions with identical eigenvalues.

Both the tuned and the detuned problems can capture instabilities characterized by spatially localized eigensolutions as $\ddot{f}_{loc}$, providing equivalent results. Of course, the detuned case would be relevant for the investigation of non-periodic non-localized modes, which could not be captured by the tuned case, but, to our knowledge, no evidence is given for the existence of such instabilities. The detuned mode $\ddot{f}_\sigma$ develops continuously from the tuned mode $\ddot{f}_{\lambda_{v,0}}$, when the detuning coefficient σ progressively deviates from zero. Excluding unlikely eigenvalue-crossing or bifurcation phenomena, it would therefore be the mode obtained from an eigenvalue tracking procedure iterating over σ and starting from the tuned solution. From this, we tend to words interpreting the results of Koch *et al.* (2000), according to which detuned modes may achieve slightly higher amplification rates than tuned ones, as a consequence of discretization errors similar to those causing deviations between our cases *Single-*$\lambda_{0,v}$ and *Double-*$\lambda_{0,v}$ in figure 17.

We conclude by documenting results for two DNS cases with identical primary states expressed in different reference systems. Since periodicity and spatial development in the DNS are always prescribed along the reference axes x and z, respectively, this provides a direct verification of the general results presented above. The set-up of case *Adapted-vortex-oriented* has been presented in § 6.1. In case *Adapted-plate-oriented* the same three-dimensional base flow (i.e. the primary state) was expressed with respect to a plate-oriented coordinate system $(\breve{\breve{x}}, y, \breve{\breve{z}})$ with $\breve{\breve{\varphi}} = 0$, which was possible since the base flow from case *Adapted-vortex-oriented* is periodic in $\breve{z}$ and constant in $\breve{x}$, and thus periodic also in any other direction, including $\breve{\breve{z}}$. A sketch of the configurations considered in the two DNS cases is provided in figure 18. Results for amplification rates and streamwise wavenumbers are compared in figure 19 and found to be nearly identical. In the DNS frame, the relative shift of the single-maximum eigenfunctions, i.e. the value of ξ in (6.4), is determined by the orientation of the perturbations strip (parallel to the $\breve{z}$ or $\breve{\breve{z}}$-axis) where all superposed eigenfunctions possess the same initial amplitude.

6.3. *Influence of modifications in* v_v *and* w_v

The relevant deviations between the v_v-fixed and the w_v-approaches demonstrate the high sensitivity of secondary amplification rates to small modifications of the primary-state velocity components $\dot{v}_v$ and $\dot{w}_v$ normal to the primary-vortex axis. We investigated this issue systematically, scaling the velocity components $\dot{v}_v$ and $\dot{w}_v$ of the primary state in the plane normal to the main vortex axis. The reference primary state was defined according to the w_v-fixed approach. Results are presented in figures 20 and 21.

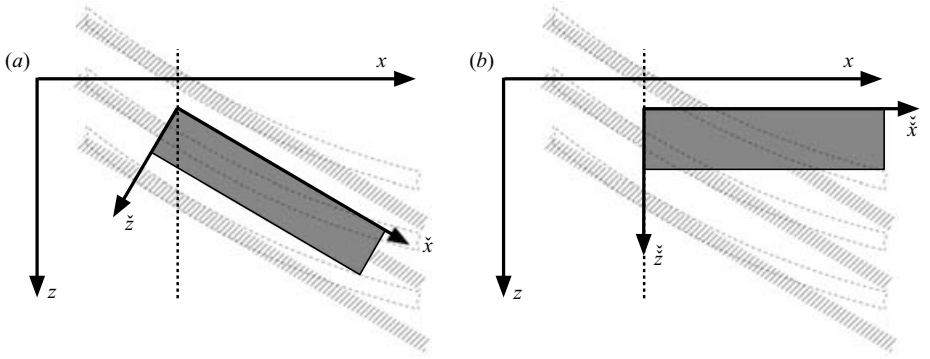

FIGURE 18. Reference systems, integration domains (grey), and schematic representation of the primary vortices (hatched) for (*a*) case *Adapted-vortex-oriented* and (*b*) case *Adapted-plate-oriented*. Dashed lines represent the plane $x = x_{SLST}$.

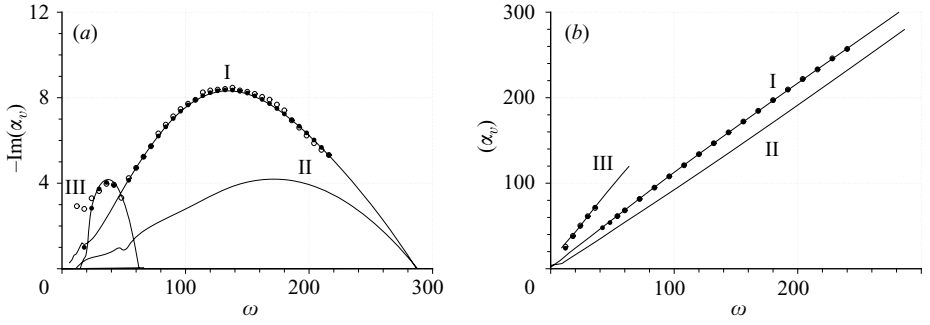

FIGURE 19. (*a*) Spatial amplification rates and (*b*) wavenumbers in the $\check{x} = x_v$ direction ($\check{\varphi} = \varphi_v = 45.86°$) from SLST (lines), from case *Adapted-vortex-oriented* (dots) and from case *Adapted-plate-oriented* (circles) as functions of the frequency. The primary state for the SLST and the three-dimensional base flows for the DNS have been defined according to the w_v-fixed approach.

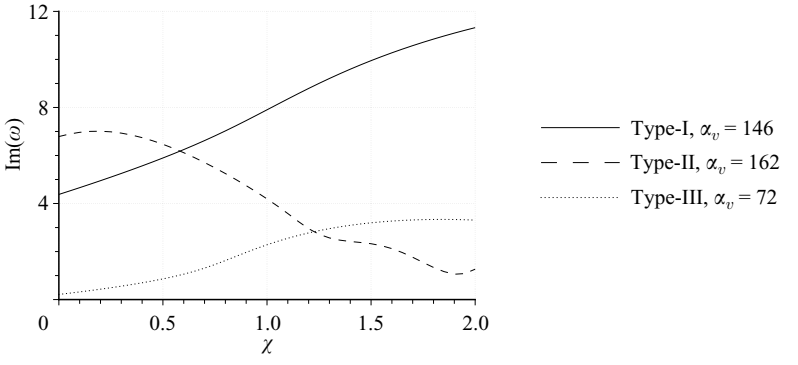

FIGURE 20. Temporal amplification rates as a function of the scaling factor χ multiplying $\dot{v}_v$ and $\dot{w}_v$. For scaled velocity components $\dot{f}$ holds $\dot{f} = \chi \dot{f}_0$, where $\dot{f}_0$ is the corresponding component of the reference primary state, defined according to the w_v-fixed approach.

The high sensitivity of the problem is confirmed and deviations from the reference case of over 50% are observed when the scaling factor χ falls to zero, which is in agreement with findings by Malik & Chang (1994). The dependency of the

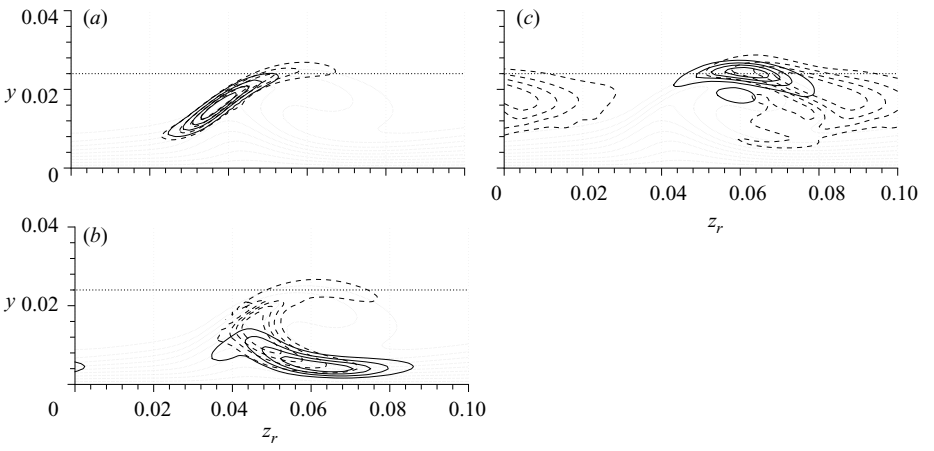

FIGURE 21. Normalized $\ddot{u}_r$-amplitude distributions ($\Delta = 0.2$) for secondary modes from figure 20 for $\chi = 0.5$ (solid lines) and $\chi = 1.5$ (dashed lines). (*a*) Type I: $\mathrm{Re}(\alpha_r) \approx 146$, $\omega \approx 132$; (*b*) Type III: $\mathrm{Re}(\alpha_r) \approx 72$, $\omega \approx 36$; (*c*) Type II: $\mathrm{Re}(\alpha_r) \approx 162$, $\omega \approx 170$.

amplification rates on χ is, however, not unequivocal since type II modes behave in the opposite way to type I and type III modes. The shapes of the eigenfunctions of all modes alter significantly with the scaling factor χ.

The relation between primary state and secondary perturbation is clearly not trivial and we need a thorough understanding of the instability mechanism (see § 8) in order to justify the results presented here or to explain the strong differences in the results for the v_v-fixed and the w_v-approach. At this point, we only notice that figure 20 hints at transition control. Secondary amplification rates of the most amplified type I mode might be reduced, or even suppressed, by properly modifying the small cross-plane velocity components, which may be effectively achieved by moderate suction or blowing at the wall.

7. Structures connected to high-amplitude secondary perturbations

After having validated SLST results in the region characterized by low-amplitude secondary perturbations, the focus of the discussion is now shifted towards the later stages of the transition process. Discretization parameters for all DNS of this section were identical to those used for the simulations of §§ 5.1 and 5.2 with the exception of the spanwise discretization, which has been enhanced up to $\gamma_{max} = 21\gamma_0$ in order to improve the resolution of secondary structures in their late stages of development. SLST eigenfunctions originate from the computations of §§ 5.1 and 5.2.

7.1. *The steady fundamental case*

7.1.1. *Secondary structures induced by one single type I mode*

In order to make the connection between coherent structures and SLST modes univocal, DNS have been carried out disturbing one single frequency in each run, so that the corresponding mode could develop without interacting with other instabilities. In case *Steady+ω120*, the frequency $\omega = 120$ ($h = 20$), i.e. one of the most amplified type I modes, was perturbed at $x = 3$. Its development in the downstream direction was similar to that for case *Steady+Pulse* (figure 9).

In the λ_2-visualization of figure 22, secondary finger-like vortical structures, similar to those also observed by Wassermann & Kloker (2002), Wintergerste (2002) and

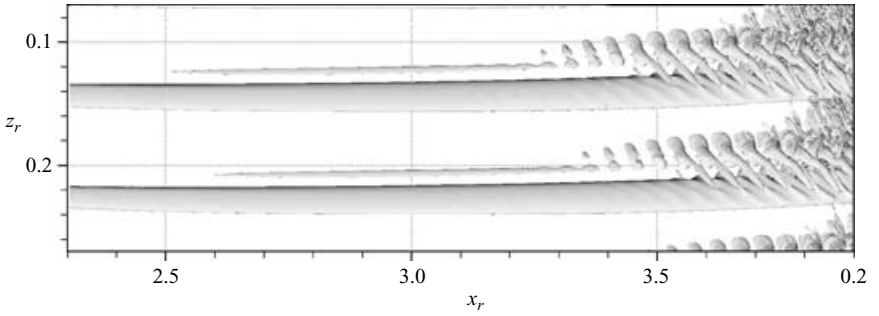

FIGURE 22. Visualization of vortical structures (λ_2-isosurfaces, $\lambda_2 = -10$) for case *Steady+ω*120: $x_{0,r} = 1.5$, $z_{0,r} = 0.10$, $\varphi_r = 45.86°$.

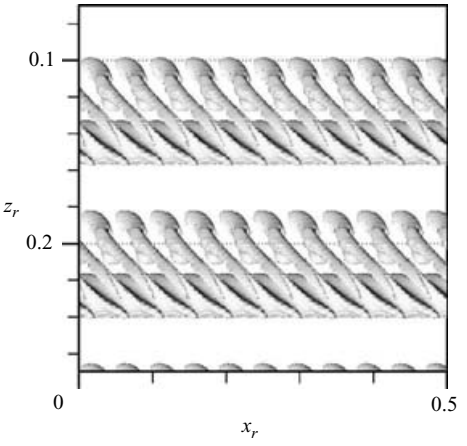

FIGURE 23. Visualization of vortical structures (λ_2-isosurfaces, $\lambda_2 = -10$) for the superposition of primary state and a type I mode ($\omega \approx 120$, $\mathrm{Re}(\alpha_v) = 134$, $max_{t,x,y,z}\{|\ddot{u}_v|\} = 0.06$) from the SLST analysis of the steady fundamental case ($x_{SLST} = 3.32$, $\varphi_v = 45.86°$).

Hein (2004) develop at the side of the primary vortex, exactly in the region where the eigenfunction of the generating mode achieves its maximal amplitude (see figures 5 and 11*a*). In contrast to the simulations by Wassermann & Kloker (2002), who initiated secondary instabilities by a multi-frequency pulse-like perturbation, and by Wintergerste (2002) and Hein (2004), who superposed steady and unsteady primary unstable modes losing the streamwise invariance of the primary state, the secondary mode preserves its streamwise quasi-periodicity up to the late stages of transition. An array of identical secondary structures convecting in the x_v-direction can be observed.

Structures similar to those of figure 22 may be found in figure 23, where the λ_2-technique has been applied to the flow field obtained by superposing the x_v-invariant primary state of the SLST analysis ($x_{SLST} = 3.32$, see figures 10 and 11) and the corresponding secondary perturbation for a type I mode with $\omega \approx 120$ and $\mathrm{Re}(\alpha_v) = 134$. Spatial amplification has been neglected and the two-dimensional eigenfunction has been scaled to finite amplitudes. The observed similarity is not trivial since nonlinear secondary-disturbance interactions and the additional primary-state distortion are neglected in the flow field of figure 23. The present results provide a legitimation *a posteriori* for visualizations by Balachandar *et al.* (1992) and Malik &

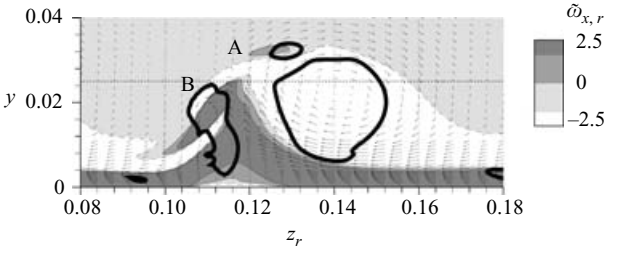

FIGURE 24. Visualization over the section plane $x_r = 3.57$ of figure 22: $[\tilde{w}_r, \tilde{v}_r]$-vectors; $\tilde{\omega}_{x,r}$-isocontours (shaded); λ_2-isocontours (thick lines, $\lambda_2 = -10$). The horizontal dotted line denotes the undisturbed boundary-layer thickness.

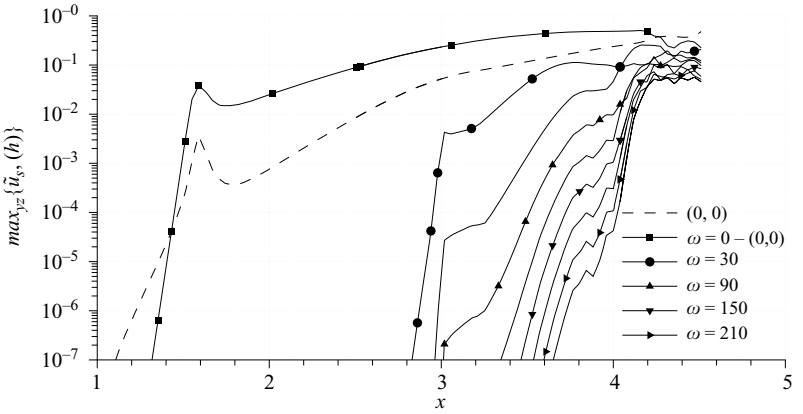

FIGURE 25. Downstream development of the modal amplitudes $\tilde{u}'_{s,(h)}$ from Fourier expansion in time (maximum over y and z, $0 \leqslant \omega \leqslant 240$, $\Delta\omega = 30$) for case *Steady+ω30* (steady fundamental case plus single low frequency).

Chang (1994), who tried to characterize secondary structures by considering finite-amplitude SLST eigenfunctions.

Further insight into the features of the secondary structures of figure 22 is provided in figure 24. Contour plots of the streamwise vorticity $\tilde{\omega}_{x,r}$ are shown over the plane $x_r = 3.57$ of figure 22 together with crosscuts of the λ_2-isosurface from that same figure and a vector plot for the in-plane component of the velocity. Clearly visible are the crosscuts of λ_2-isosurfaces connected to two secondary structures. The most upstream one crosses the section plane with its upraised head (marked as A). The most downstream one is intersected in the middle of its trunk (marked as B). The streamwise vorticity associated to both secondary vortices is positive, i.e. their rotation direction is opposite to that of the primary vortex.

7.1.2. *Secondary structures induced by a single type III mode*

Flow structures induced by type III modes have been investigated in case *Steady+ω30*, where only the secondary mode $\omega = 30$ ($h = 5$) has been triggered at $x = 3$. Thereby initial amplitudes have been increased with respect to case *Steady+ω120* in order to compensate for the relatively low amplification rates of the considered mode. The streamwise development of the perturbation is shown in figure 25. Type III modes are clearly not as efficient as type I modes in triggering the laminar

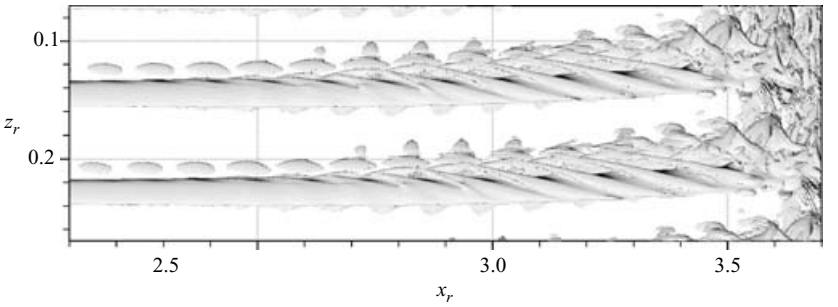

FIGURE 26. Visualization of vortical structures (λ_2-isosurfaces, $\lambda_2 = -10$) for case *Steady+ω30*: $x_{0,r} = 1.5$, $z_{0,r} = 0.10$, $\varphi_r = 45.86°$.

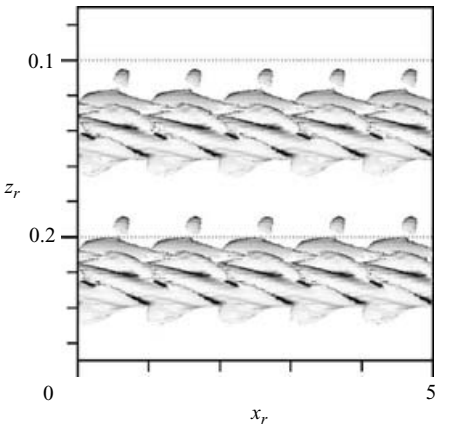

FIGURE 27. Visualization of vortical structures (λ_2-isosurfaces, $\lambda_2 = -10$) for the superposition of primary state and a type III mode ($\omega \approx 30$, $\mathrm{Re}(\alpha_v) = 62$, $max_{t,x,y,z}\{|\tilde{u}_v|\} = 0.12$) from the SLST analysis of the steady fundamental case ($x_{SLST} = 3.32$, $\varphi_v = 45.86°$).

breakdown, which indeed does not take place before $x = 4.2$ and is not initiated by mode $\omega = 30$, but rather by its first superharmonic $\omega = 60$, which is already of type I.

A λ_2-visualization of case *Steady+ω30* is shown in figure 26. The primary vortex is strongly deformed into a rope-like structure with different vortical filaments winding around the main core. A comparison of figures 26 and 27 confirms that also in this case qualitative similarity is given between the real structures and those obtained by visualizing finite-amplitude modal eigenfunctions from the SLST.

The rotation directions of the vortex filaments building up the rope-like structure of figure 26 is made evident by the contour plot of the streamwise vorticity shown in figure 28 for the plane $x_r = 3.57$. Even if crosscuts of λ_2-isosurfaces associated with filaments characterized by both positive (marked as A and B) and negative $\omega_{x,r}$ (marked as C, D and E) can be found, the most evident structures in figure 26 are those possessing negative streamwise vorticity, i.e. rotating in the same direction as the main vortex.

7.2. *Unsteady fundamental case*

7.2.1. *Secondary structures induced by a single type I mode*

Secondary structures associated with a high-amplitude type I mode in the unsteady fundamental case are visualized in figure 29. The flow field originates from the

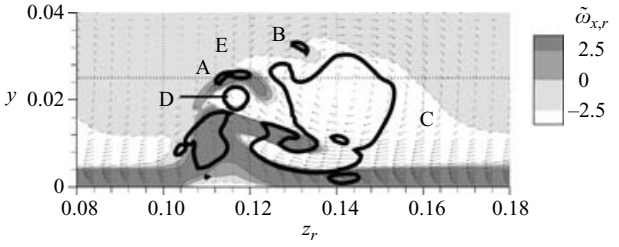

FIGURE 28. Visualization over the section plane $x_r = 3.57$ of figure 26: $[\tilde{w}_r, \tilde{v}_r]$-vectors; $\tilde{\omega}_{x,r}$-isocontours (shaded); λ_2-isocontours (thick lines, $\lambda_2 = -10$). The horizontal dotted line denotes the undisturbed boundary-layer thickness.

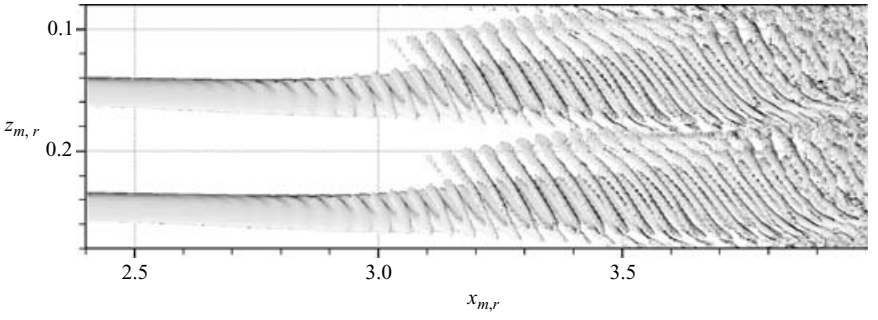

FIGURE 29. Visualization of vortical structures (λ_2-isosurfaces, $\lambda_2 = -10$) for case *Unsteady+ω_m120*: $x_{0,m,r} = 1.5$, $z_{0,m,r} = 0.07$, $\varphi_{m,r} = 37.77°$.

DNS case *Unsteady+ω_m120*, where only the frequency $\omega_m = 120$ ($h_m = 20$) has been perturbed at $x_m = 3$. The downstream development of the excited mode was similar to that documented for case *Unsteady+Pulse* (figure 12). Secondary vortical structures are visualized in figure 29, where analogies can be found with respect to structures from type I instabilities of the steady fundamental case (figure 22). However, the present structures, when considered in the plate-fixed coordinate system, convect in the downstream direction and also follow the motion of the primary unsteady vortices shifting in the z-direction. In the moving system chosen for the visualization, they convect only in $x_{m,r}$-direction. Again, good agreement is observed between real structures and structures from finite-amplitude secondary modes visualized in figure 30. Finally, figure 31 shows the rotation sense of the main secondary structures, which is opposite to that of the primary vortex even if smaller co-rotating structures are also present.

8. Interpretation of the instability mechanism

The characterization presented above for structures originated by secondary unstable modes provides a basis for the interpretation of the instability mechanism. Again, we refer only to the steady fundamental case.

We claim that the instability mechanism for secondary CF instabilities is analogous to the inviscid Kelvin–Helmholtz instability of the plane step-profile mixing layer (see Drazin & Reid 2004) or to the shear-layer instability of the tanh-profile mixing layer (Michalke 1964) and of jet flows (Michalke 1982). A substantiation of this hypothesis is provided in the following by showing that characteristic features of the Kelvin–Helmholtz scenario may be found also in the flow field associated to secondary CF instabilities.

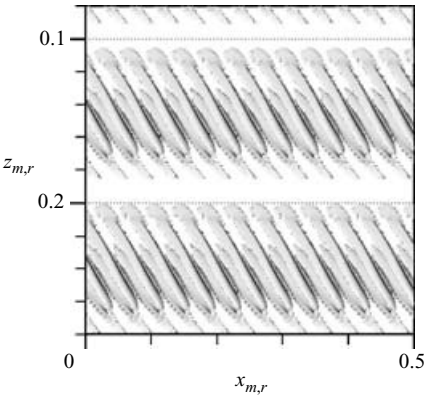

FIGURE 30. Visualization of vortical structures (λ_2-isosurfaces, $\lambda_2 = -10$) for the superposition of primary state and a type I mode ($\omega_m \approx 120$, $\mathrm{Re}(\alpha_{m,v}) = 148$, $max_{t,x,y,z}\ \{|\ddot{u}_{m,v}|\} = 0.12$) from the SLST analysis of the unsteady fundamental case ($x_{m,SLST} = 3.32$, $\varphi_{m,v} = 37.77°$).

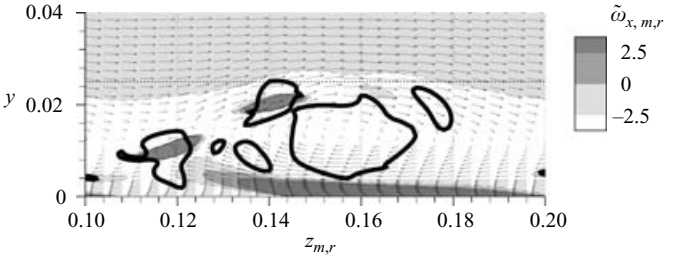

FIGURE 31. Visualization over the section plane $x_{m,r} = 3.21$ of figure 29: $[\tilde{w}_{m,r}, \tilde{v}_{m,r}]$-vectors; $\tilde{\omega}_{x,m,r}$-isocontours (shaded); λ_2-isocontours (thick lines, $\lambda_2 = -10$). The horizontal dotted line denotes the undisturbed boundary-layer thickness.

8.1. *Identification of the vorticity layer*

The unstable element in the step-profile mixing-layer is represented by a plane infinitely thin vorticity layer at the boundary between two uniform streams with different velocities. When an infinitesimal deflection from its plane configuration is introduced, a self-induced process leads to the concentration of vorticity into discrete straight co-rotating vortex cores, i.e. local maxima of the vorticity field associated to eigensolutions of the stability problem, all of which lie in the plane of the original layer. With regard to secondary CF instabilities, vortex cores associated to modal eigenfunctions have been visualized in figures 23 and 27 for type I and type III modes, respectively. For the analogy with the Kelvin–Helmholtz instability to hold, a vorticity layer should exist in the flow field associated to the primary state. The vorticity component tangent to the vortex cores (referred to as $\dot{\omega}_{x,t}$ in the following) should be maximal in the neighbourhood of the cylindrical surface with generatrices parallel to the primary-vortex axis (x_v-direction) and cutting across the secondary vortex cores.

We determined the orientation of the secondary-vortex cores using a post-processing tool by Linnick & Rist (1999), in which vortex cores are extracted from a given flow field by tracking local minima in the corresponding λ_2-field (Jeong & Hussain 1995). The procedure was applied to flow fields associated to eigenfunctions from all three instability types (figure 32). Classical λ_2-visualizations of the flow field resulting from the superposition of the secondary eigenfunctions and the primary state are shown in

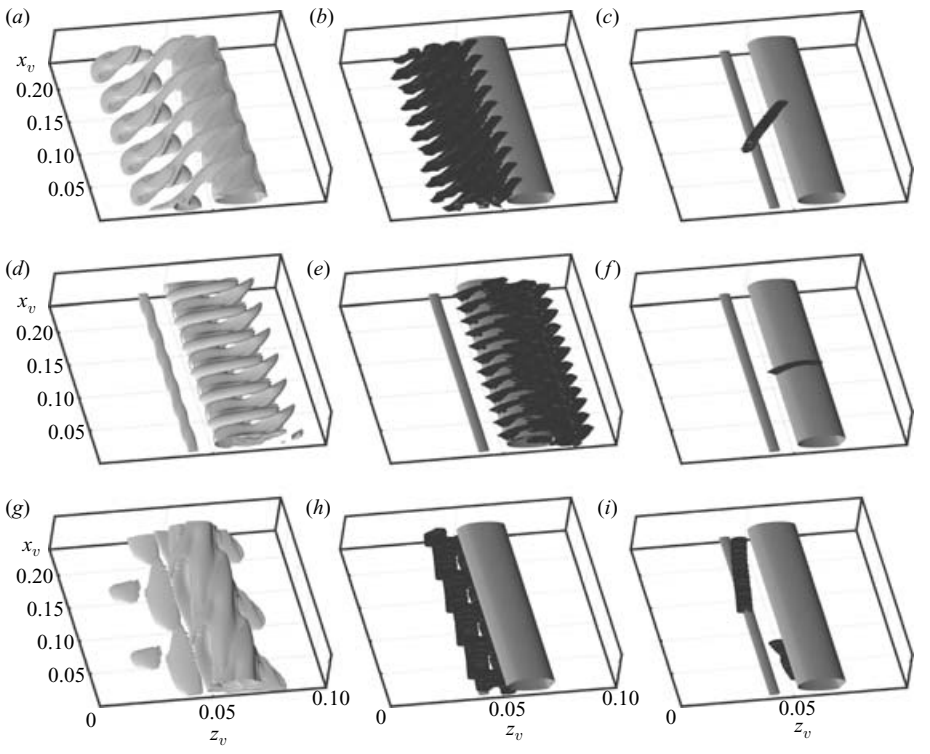

FIGURE 32. Secondary-vortex cores for type I (*a–c*, $\mathrm{Re}(\alpha_v) = 134$), type II (*d–f*, $\mathrm{Re}(\alpha_v) = 162$) and type III (*g–i*, $\mathrm{Re}(\alpha_v) = 62$). Left column: perspective view of the λ_2 isosurfaces from the flow field obtained superposing primary state and finite-amplitude secondary eigenfunctions ($\lambda_2 = -10$). Central column: vortex cores from the secondary-perturbation flow field (black surfaces) and λ_2-isosurface for the primary vortex (grey surface, $\lambda_2 = -10$). Right column: selected cores for further analysis (black surfaces) and λ_2-isosurface for the primary vortex (grey surface, $\lambda_2 = -10$). The maximal amplitude $max_{t,x,y,z}\{|\ddot{u}_v|\}$ of the secondary eigenfunctions was 0.06 for type I and type II modes, 0.12 for type III modes.

left column (figure 32). The extracted vortex cores are visualized in the central column, and the most significant one of each case, considered in the following for further analysis, is shown in the right column. The choice of the structure to be investigated is to some extent an arbitrary process. We selected well-developed structures, whose shapes were closest to that of the structures from the λ_2-visualization of the global flow field. It is also worth mentioning that visualizations in the central column of figure 32 present a streamwise periodicity with twice as many structures as in the visualizations in the left column. Indeed, for each local extremum in the perturbation vorticity there is always a corresponding identical extremum with opposite sign, shifted in x_v by half a wavelength. The vortex extraction procedure applied to the perturbation flow identifies corresponding structures of extrema of both signs, but in the global flow field only extrema enhancing the vorticity layer from the primary state effectively lead to a secondary structure.

Components of the primary-state vorticity field in the direction parallel to the secondary vortex cores are shown in figure 33. Since the vortex-core orientation varies moderately over the length of type I and type II structures, only one representative direction is considered in such cases. On the contrary, three different orientations are

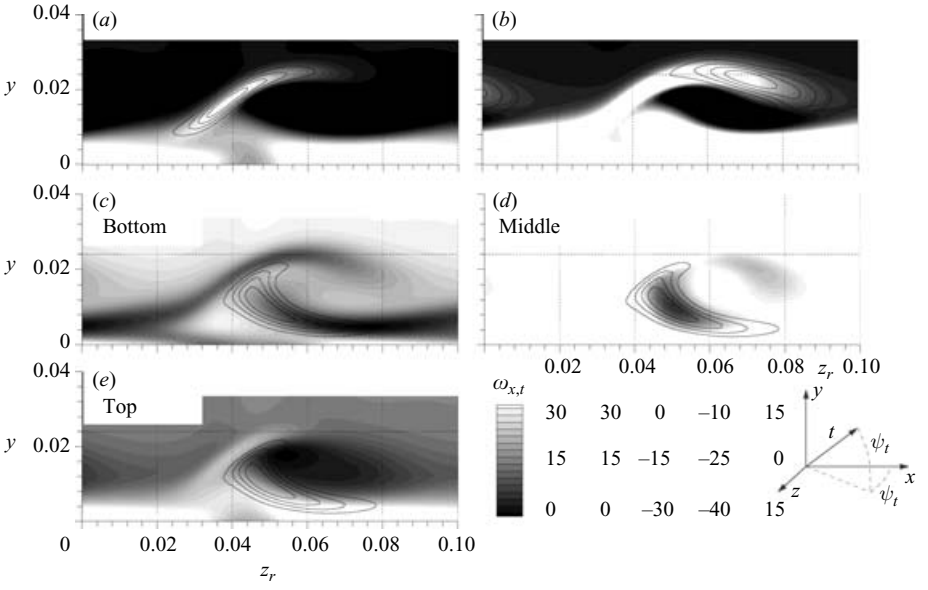

FIGURE 33. Vorticity component $\dot{\omega}_{x,t}$ of the primary flow (shaded) along the direction t parallel to the vortex cores of the secondary structures from figure 32. The crosscut plane is normal to the primary-vortex axis ($\varphi_r = \varphi_v = 45.86°$). See sketch in figure for the definition of the angles φ_t and ψ_t determining the direction t. Three different orientations of the vortex core are considered for the type III structure. The orientation of the central section (d) has been approximately estimated since the vortex-core-extraction procedure did not work there. Normalized amplitudes of the modal eigenfunctions from figure 11 are also plotted (lines, $\Delta = 0.2$). (a) Type I: $\varphi_t = \varphi_v + 18°$, $\varphi_t = 12°$; (b) type II: $\varphi_t = \varphi_v + 75°$, $\psi_t = -25°$; (c) type III: $\varphi_t = \varphi_v - 11.5°$, $\psi_t = 5.7°$; (d) type III: $\varphi_t = \varphi_v$, $\psi_t = 60°$; (e) type III: $\varphi_t = \varphi_v + 5.8°$, $\psi_t = 5.7°$.

considered for the type III structure, one for the bottom (upstream) portion of the structure trunk, one for the middle portion and one for the top (downstream) portion. In all figures, isocontours of the normalized eigenfunction amplitudes are reported for the corresponding secondary modes. According to the analogy with the Kelvin–Helmholtz instability, the conjectured vorticity layer should cut through the amplitude maxima of the secondary eigenfunction. The matching is evident in the case of the type I and type II modes, for which the secondary eigenfunctions are centred on marked vorticity maxima. As far as the type III mode is concerned, the situation is clear for the bottom and middle sections, where the eigenfunction is overlaid on a minimum of the vorticity field, but also, in the top region, the upper part of the eigenfunction lies in a dark region (negative $\dot{\omega}_{x,t}$) enclosed between two lighter regions (less negative $\dot{\omega}_{x,t}$).

8.2. *Reynolds number dependence*

For an instability mechanism analogous to the inviscid Kelvin–Helmholtz instability, we would expect viscosity to play a mainly damping role. Figure 34 shows the dependence on the Reynolds number Re of the temporal amplification rates for the secondary modes from figure 11. In all computations, the primary state was kept constant for varying Re and equal to the one extracted from the DNS flow field for the original value $Re = 9.2 \times 10^4$. The modified Reynolds number entered only into the computation of the secondary perturbation. Again, type I and type II instabilities perfectly fulfil the expectations presenting monotonously growing amplification rates. On the contrary, the type III mode, reaches a maximum in the amplification and then stabilizes, becoming damped for $Re > 3.8 \times 10^5$. In support of a connection

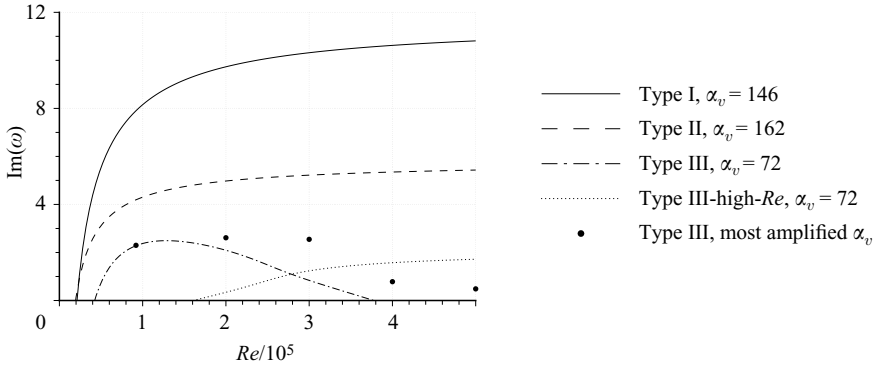

FIGURE 34. Temporal amplification rates as a function of Re. The primary state has been extracted according to the w_v-fixed approach from the DNS flow field ($Re = 9.2 \times 10^4$) and is kept constant for Re varying in the SLST analysis.

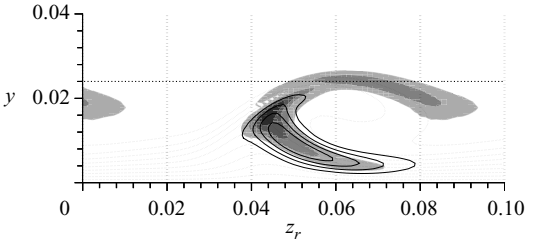

FIGURE 35. Normalized $\ddot{u}_v$-amplitude distributions of the type III mode for the most amplified wavenumbers at $Re = 5 \times 10^5$ ($\mathrm{Re}(\alpha_v) = 56$, shaded, $\Delta = 0.2$) and $Re = 9.2 \times 10^4$ ($\mathrm{Re}(\alpha_v) = 72$, lines, $\Delta = 0.2$). The crosscut plane is normal to the primary-vortex axis ($\varphi_v = 45.86°$). The primary state for the SLST has been extracted according to the w_v-fixed approach. The horizontal dotted line denotes the undisturbed boundary-layer thickness.

with an inviscid instability mechanism remains the fact that maximal amplification rates (maximum over α_v for constant Re, symbols in figure 34) decrease, but remain positive for arbitrarily large Re. Furthermore, we also found a second type III mode which becomes unstable only for relatively large Re, but then shows monotonously growing amplification rates (type III-high-Re in figure 34).

Eigenfunctions for type I and type II modes remain practically unvaried over the considered Re-range and need not be displayed. The amplitude distribution of the type III mode for the most amplified streamwise wavenumber $\alpha_v = 56$ at $Re = 5 \times 10^5$ is documented in figure 35, where also the eigenfunction from figure 11 ($Re = 9.2 \times 10^4$, $\alpha_v = 72$) is plotted for reference. Maximum amplitudes move away from the wall for increasing Re, so that viscosity appears to be relevant in determining the development of the instability in the near-wall region. Furthermore, a second amplitude maximum similar to a type II mode appears in the eigenfunction, which is interesting since, as one may see in figure 33, type II and type III develop from vorticity layers with opposite sign. Eigenfunctions for the type III-high-Re mode are qualitatively similar to the one displayed in figure 35.

8.3. *Dependence on the shear-layer strength*

If a scaling is applied onto the shear-layer profile of the Kelvin–Helmholtz problem, the resulting eigenvalues, i.e. the amplification rates and frequencies of the instabilities, depend linearly on the scaling factor. The persistence of this behaviour in the

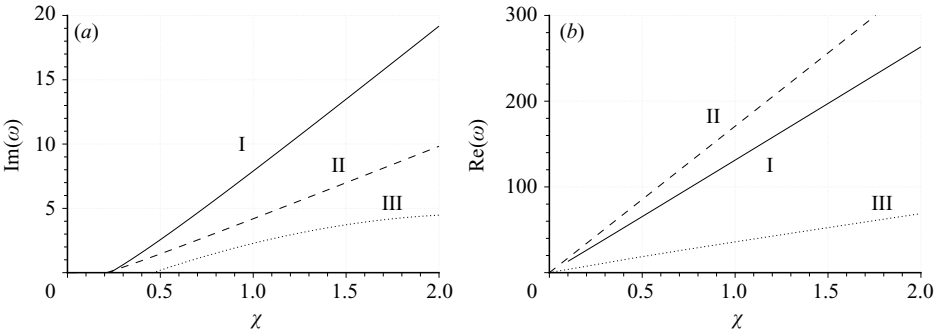

FIGURE 36. (*a*) Temporal amplification rates and (*b*) angular frequencies of the unstable modes from figure 11 (fixed streamwise wavenumber) as functions of the scaling factor χ multiplying all three components of the primary state. The reference primary state has been extracted according to the w_v-fixed approach.

secondary-instability context may be verified by scaling simultaneously all three components $\dot{u}_v$, $\dot{v}_v$ and $\dot{w}_v$ of the primary state. Results are presented in figure 36.

The behaviour of type I and type II modes, for which amplification rates depend almost exactly linearly on the scaling factor χ, matches perfectly the proposed Kelvin–Helmholtz analogy. Deviations are observed for the type III mode. The offset from the origin for all curves in figure 36(*a*) is plausibly due to the slightly stabilizing influence of viscosity.

8.4. *Motion of the secondary vortex cores*

In the Kelvin–Helmholtz scenario, perturbations with non-zero streamwise wavenumber represent the corrugation of the unstable vorticity layer, so that their phase velocity must be equal to the convection velocity of the layer, which in turn is determined by the Kelvin and Helmholtz vortex theorems. The situation is clearest in cases with an infinitely thin vorticity layer, whose material velocity is equal to the mean velocity of the two streams.

We identify in a first approximation the finite-thickness vorticity layer of the CF scenario (see figure 33) with the cylindrical surface crossing the vortex cores of figure 32 with generatrix parallel to the x_v-axis. Furthermore, we assume each point of that surface to be convected by the primary-state velocity field. This provides a determination of the motion of the secondary vortex cores, which, if our assumptions are correct, should match the motion prescribed by the SLST model, i.e. convection in the x_v-direction with velocity equal to the phase velocity $c_{ph,v}$ of the considered mode. A first hint is provided by the results of figure 10(*b*) if we consider that, for waves convecting with a prescribed phase velocity, the angular frequency ω must be proportional to the streamwise wavenumber $\mathrm{Re}(\alpha_v)$.

Let $[x_v(s)\ y(s)\ z_v(s)]^T$ be a parameterization of the spatial curve describing any of the vortex cores from figure 32 and let $[\dot{u}_v(s)\ \dot{v}_v(s)\ \dot{w}_v(s)]^T$ be the primary-state velocity in $[x_v(s)\ y(s)\ z_v(s)]^T$. The connection between the convection-induced motion and the SLST motion requires then

$$\begin{bmatrix} c_{ph,v} \\ 0 \\ 0 \end{bmatrix} = \begin{bmatrix} \dot{u}_v(s) \\ \dot{v}_v(s) \\ \dot{w}_v(s) \end{bmatrix} + \breve{u}(s) \begin{bmatrix} t_{x,v}(s) \\ t_{y,v}(s) \\ t_{z,v}(s) \end{bmatrix}, \tag{8.1}$$

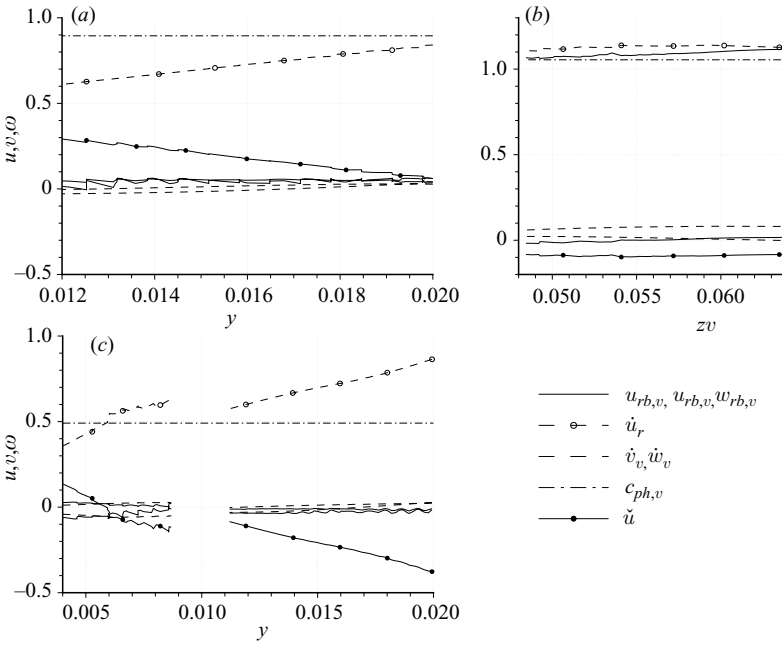

FIGURE 37. Primary-state velocity components and rigid-body velocity components (right-hand side of (8.1)) at points of the vortex cores from figure 32. The function $\breve{u}$ is computed imposing the x_v-component of (8.1) for type I and type III modes, and the z_v-component for the type II mode. The component of the rigid-body velocity directly determined by (8.1) is not plotted. The variable on the abscissa is different in different figures. (*a*) Type I, $\mathrm{Re}(\alpha_v) = 134$, $c_{ph,v} = 0.89$; (*b*) type II, $\mathrm{Re}(\alpha_v) = 162$, $c_{ph,v} = 1.05$; (*c*) type III, $\mathrm{Re}(\alpha_v) = 62$, $c_{ph,v} = 0.49$.

where $\breve{u}(s)$ is a scalar function and $[t_{x,v}(s)\ t_{y,v}(s)\ t_{z,v}(s)]^T$ is the unity vector tangent to the core line in $[x_v(s)\ y(s)\ z_v(s)]^T$. The tangent velocity $\breve{u}$ may be determined arbitrarily since it only represents a relative motion of the different points of the vortex core along the core line itself. It does not affect the shape, the position, and consequently the motion, of the vortex core as a whole.

We determined $\breve{u}(s)$ from the component of (8.1) associated to the largest component of the tangent vector $[t_{x,v}(s)\ t_{y,v}(s)\ t_{z,v}(s)]^T$ ($t_{x,v}$ for type I and type III modes, $t_{z,v}$ for type II modes) and verified that the remaining components of the equation were also fulfilled. The most relevant quantities involved in (8.1) are plotted in figure 37, where the rigid-body motion $[u_{rb,v}(s)\ v_{rb,v}(s)\ w_{rb,v}(s)]^T$ represents the right-hand side of (8.1), $\breve{u}$ having been determined as described above. Considering the approximation due to the finite thickness of the vorticity layer, the fulfilment of (8.1) is in all cases satisfactory. The y_v and z_v components of the right-hand side of (8.1) are close to zero and, for the type II mode, the x_v-component gives a good approximation of the phase velocity of that mode. The wiggly behaviour of some curves is due to oscillations of the vortex-core tangents from the extraction procedure.

8.5. *Dependence on primary-state features other than the main shear layer*

The Kelvin–Helmholtz analogy also provides an explanation for the sensitivity of SLST results with respect to modifications of the primary state, i.e. for the deviations between SLST and DNS in § 5 and the results of § 6.3. We illustrate two mechanisms, through which alterations in velocity components not directly connected to the main shear layer may induce comparatively large deviations in the secondary amplification

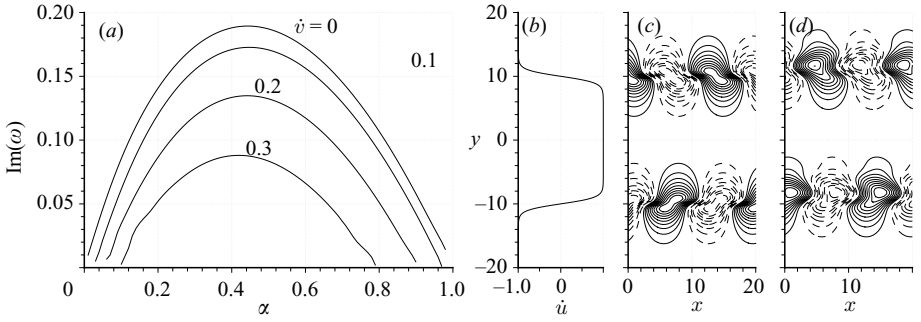

FIGURE 38. Temporal amplification rates for (*a*) different values of $\dot{v}$, (*b*) base flow profile $\dot{u}$, and normalized $\ddot{v}$-eigensolutions for (*c*) $\alpha=0.45$, $\dot{v}=0.0$ and (*d*) $\alpha=0.45$, $\dot{v}=0.2$. Dashed lines in (*c*) and (*d*) correspond to negative values, isolines $\ddot{v}=0$ are not plotted, $\Delta=0.1$.

rates. Plausibility checks on the basis of the results from the previous sections are also provided. The discussion concentrates on type I and type II modes, for which the Kelvin–Helmholtz analogy has been found to match more exactly.

8.5.1. *Stabilizing effect of a velocity component normal to the main shear layer*

In order to allow quantitative comparisons, we solved an artificial Kelvin–Helmholtz stability problem with (periodic) tanh profile in the (x, y)-plane and a superimposed constant velocity component in the direction normal to the main shear layer. The unperturbed base flow was

$$\dot{u}(x, y)=\sum_{k=-\infty}^{+\infty}(-1)^k \tanh\left[y-\left(k-\tfrac{1}{2}\right)\times 20\right], \qquad \dot{v}(x, y)=K\in\mathbb{R}, \tag{8.2}$$

which corresponds to two antisymmetric tanh profiles in $y=\pm 10$, periodically repeated with a fundamental wavelength of $\lambda_y=40$. The perturbation velocities $\ddot{u}$ and $\ddot{v}$ were assumed to have the form

$$\ddot{f}(t, x, y)=2\mathrm{Re}[\hat{\ddot{f}}(y)\exp(\mathrm{i}(\alpha x-\omega t))], \qquad \alpha\in\mathbb{R},\ \omega\in\mathbb{C}, \tag{8.3}$$

where $\hat{\ddot{f}}(y)$ is a complex periodic function. The stability problem was solved according to the temporal approach considering the eigenvalue problem

$$-\mathrm{i}\omega\Delta\hat{\ddot{v}}+\dot{u}\frac{\partial\Delta\hat{\ddot{v}}}{\partial x}+\dot{v}\frac{\partial\Delta\hat{\ddot{v}}}{\partial y}-\frac{\partial^2\dot{u}}{\partial y^2}\frac{\partial\hat{\ddot{v}}}{\partial x}=0, \qquad \Delta=-\alpha^2+\frac{\partial^2}{\partial y^2}. \tag{8.4}$$

Discretization in the y-direction was achieved by means of Fourier expansions with 256 harmonics.

Results are presented in figure 38. A significant reduction of the amplification rates can be observed for increasing $\dot{v}$, which can be intuitively explained considering that $\dot{v}$ tends to convect the unstable vortex cores away from the shear layer, into a region of the flow field where they are stable. The shape of the $\ddot{v}$-eigenfunctions is only moderately affected.

A proper scaling is required in order to close the comparison between the Kelvin–Helmholtz scenario and the secondary instability of CF vortices. For each problem we defined an equivalent velocity jump $\Delta\dot{u}_{eq}$ proportional to the shear-layer thickness h (estimated by visual inspection of figures 33 and 38*b*) and to the maximum absolute value $\dot{\zeta}_{max}$ of the vorticity component $\dot{\zeta}$ normal to the shear layer ($\dot{\zeta}=\dot{\omega}_z$ for the

	$\dot{v}=0.0$	$\dot{v}=0.1$	$\dot{v}=0.2$	Type I	Type II
$\dot{\zeta}_{max}$	1	1	1	30	35
h	4	4	4	0.005	0.007
$\Delta\dot{u}_{eq}=\dfrac{\dot{\zeta}_{max}h}{4}$	1	1	1	0.037	0.061
$\dfrac{\Delta\dot{v}_{n,max}}{\Delta\dot{u}_{eq}}$				0.11	0.0065
$\dfrac{\mathrm{Im}(\omega)_{max}}{\dot{\zeta}_{max}}$	0.19	0.17	0.13	0.17; 0.26†	0.12; 0.12†
$\alpha_{max}h$	1.80	1.80	1.76	2.01; 2.09†	1.12; 1.25†

† Values for the SLST modes refer to the v_v-fixed and the w_v-fixed approaches, respectively.

TABLE 1. Rescaled quantities from the Kelvin–Helmholtz problems ($\dot{v}=0.0$, $\dot{v}=0.1$ and $\dot{v}=0.2$) and from the SLST problems for the type I and type II modes of figure 10.

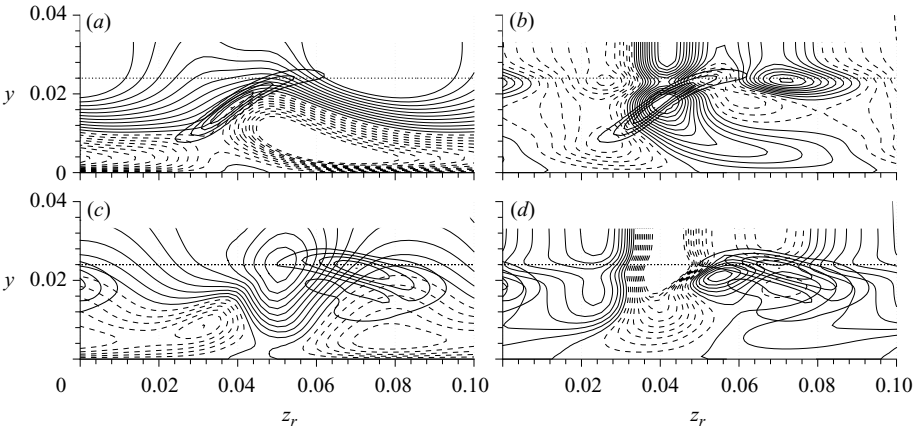

FIGURE 39. Primary-state component $\dot{v}_n$ normal to the shear layer connected to the type I (*a*, *b*) and type II (*c*, *d*) structures of figures 32 and 33. The angles φ_n and ψ_n (see figure 33 for definition) define the direction of $\dot{v}_n$. (*a*, *c*) $\dot{v}_n$ according to the w_v-fixed approach ($\Delta=0.004$). $\dot{v}_n$ from the w_v-fixed approach minus $\dot{v}_n$ from the v_v-fixed approach ($\Delta=0.0004$). Dashed lines correspond to negative values, thick lines give the eigenfunction associated to the considered structures. (*a*) $\dot{v}_n : \varphi_n=\varphi_v=90°$, $\psi_n=-55.5°$; (*b*) $\Delta\dot{v}_n : \varphi_n=\varphi_v+90°$, $\psi_n=-55.5°$; (*c*) $\dot{v}_n : \varphi_n=\varphi_v+90°$, $\psi_n=74.5°$; (*d*) $\Delta\dot{v}_n : \varphi_n=\varphi_v+90°$, $\psi_n=74.5°$.

Kelvin–Helmholtz base flow, $\dot{\zeta}=\dot{\omega}_{x,t}$ for the SLST primary state, see figure 33). We then expect results from all problems to collapse if velocities are scaled with $\Delta\dot{u}_{eq}$, lengths with h and temporal eigenvalues with $\dot{\zeta}_{max}$.

Quantitative data are provided in table 1. Thereby $\dot{v}_n$ is the velocity component normal to the shear layer in the SLST primary states and $\Delta\dot{v}_{n,max}$ is the deviation between the flow fields defined according to the v_v-fixed and the w_v-fixed approaches in the regions of interest by the corresponding secondary eigenfunctions (see figure 39). Maximal amplification rates $\mathrm{Im}(\omega)_{max}$ and the associated wavenumbers α_{max} are also provided. For CF modes, the direction n is defined as the normal to the x_v-axis and to the secondary vortex cores from figures 32 and 33. The wavenumber α is computed for the direction q normal to the vortex cores and lying in the shear-layer

plane ($\alpha = \alpha_q = \alpha_v / \cos\varphi_{v,q}$, where $\varphi_{v,q}$ is the angle spanned by the x_v-axis and the q-direction).

The relatively large value of $\Delta\dot{v}_{n,max}/\Delta\dot{u}_{eq} = 0.11$ for the type I mode might well be responsible for the differences between amplification rates from the v_v-fixed and the w_v-fixed approaches. To a 38%-variation in $\mathrm{Im}(\omega)_{max}$ between the two SLST approaches corresponds an 8% variation between Kelvin–Helmholtz problems with $\dot{v}/\Delta\dot{u}_{eq} = 0.0$ and $\dot{v}/\Delta\dot{u}_{eq} = 0.1$ and a 21% variation between problems with $\dot{v}/\Delta\dot{u}_{eq} = 0.1$ and $\dot{v}/\Delta\dot{u}_{eq} = 0.2$. Notice that v_n in figure 39(a) is only approximately zero in the region of interest. On the other hand, the negligible value of $\Delta\dot{v}_{n,max}/\Delta\dot{u}_{eq}$ for the type II mode explains the moderate sensitivity of that mode with respect to the definition of the primary state. Finally, the order-of-magnitude matching between amplification rates and wavenumbers for Kelvin–Helmholtz and CF instabilities confirms the correctness of the scaling, and of the analogy it relies on. In consideration of the approximated character of the scaling procedure, better agreement cannot be expected.

8.5.2. *Modification of the vortex-core orientation*

If alterations in the primary state are significant, a further mechanism becomes relevant in determining the behaviour of the secondary instability. We notice that the orientation of the unstable vortex cores is not given a priory in the SLST problem, but rather is determined by the interplay of the unstable three-dimensional shear layer embedded in the primary state and the rigid-body-motion requirement discussed in § 8.4. The shear layer may be unstable with respect to vortex cores associated to a wide range of orientations, but only vortical elements for which (8.1) may be fulfilled are eligible for exponential growth. Scaling $\dot{v}_v$ and $\dot{w}_v$ as in § 6.3, for example, does not modify significantly the intensity of the shear layer, which is mainly connected with the $\dot{u}_v$-component, but does determine deviations in the orientation of the vortical cores fulfilling the rigid-body-motion condition. Since only the intensity of the shear layer in the plane normal to the vortical core is in a first approximation relevant for the instability, the amplification rates also vary with the scaling factor χ. The connection between primary state, vortex-cores orientation, and secondary amplification rates is not easily predictable and it is therefore not surprising that amplification rates for type I and type II modes behave in opposite ways in figure 20. Of course, the effect discussed above of alterations in the primary-state velocity component normal to the shear layer should also be considered.

Two aspects of the result from § 6.3 may be adduced to confirm what has been said. First, the relevant alterations in the eigenfunction shape in figure 21 is a clear indication of modifications in the structure (shape, orientation) of the unstable vortex cores. Secondly, we evaluated the orientation of the secondary vortex cores for the type I mode and found a deviation of the tangent direction t from $\varphi_t = \varphi_v + 18°$, $\psi_t = 12°$ for $\chi = 1.0$ (see figure 32a) to $\varphi_t = \varphi_v + 23°$, $\psi_t = 15°$ for $\chi = 2.0$. Correspondingly, the maximum $\dot{\zeta}_{max}$ of the vorticity component $\dot{\omega}_{x,t}$ within the region covered by the secondary eigensolution increased by 26% (from $\dot{\zeta}_{max} = 30$ to $\dot{\zeta}_{max} = 37$, different orientations of t for different values of χ). This corresponds to an increase in the effective shear-layer strength seen by the unstable vortex cores, which is in line with and partially justifies the 48%-increase in the amplification rates. It is also worth mentioning that the maximal value of $\dot{\omega}_{x,t}$ computed for the fixed original direction $\varphi_t = \varphi_v + 18°$, $\psi_t = 12°$ decreases monotonously for increasing χ, which makes it impossible to explain the increase in the amplification rates without considering changes in the vortex-core direction.

8.6. *Conclusions on the Kelvin–Helmholtz analogy*

The analogy with the inviscid Kelvin–Helmholtz instability mechanism holds most closely for type I and type II secondary modes, while viscous effects seem to be not negligible for type III modes. However, similarities with the Kelvin–Helmholtz scenario have been found also for this instability type, so that the superposition of viscous effects does not seem to exclude the existence of an underlying inviscid mechanism. We list relevant features of the crossflow secondary instability, which can easily be explained under consideration of the Kelvin–Helmholtz analogy.

(*a*) Linearity of the dispersions (figures 10*b* and 12*b*). The motion of secondary perturbations is determined by the motion of the originating vorticity layer. As a result phase velocities are equal for all instabilities developing in the same region (§ 8.4).

(*b*) Local character of the instability. Any vorticity layer at the side of any primary vortex is unstable by itself, without the need for interaction with neighbouring layers. Neither is periodicity in the streamwise direction necessary. Localized corrugation of the shear layer may well result in a limited number of unstable vortex cores, as in the DNS by Wassermann & Kloker (2002).

(*c*) Similarity of the secondary instability for steady and unsteady primary states (§§ 5.1 and 5.2). For the Kelvin–Helmholtz instability, it is irrelevant whether the unstable shear layer is fixed or translating with constant velocity.

(*d*) Shape and orientation of secondary structures. Unstable vortex cores must lie within a primary-state shear layer and be so oriented as to ensure the realizability of a rigid-body motion (§§ 8.4 and 8.5.2).

(*e*) Sensitivity of secondary amplification rates on small alterations in the primary state. This is a consequence of the sensitivity of the Kelvin–Helmholtz instability with respect to velocity components normal to the main shear layer (§ 8.5).

(*f*) Strength of the instability. Amplification rates are proportional to the strength of the shear layer projected onto the plane normal to the vortex cores. The instability is reduced in the presence of velocity components normal to the shear layer (§§ 8.1 and 8.5.1).

In conclusion, the $\tilde{\omega}_{x,r}$-distribution in figure 5(*e*) is mostly determined by the gradient $\partial w_r/\partial y$ rather than by $\partial v/\partial z_r$. The better performance of the w_v-fixed approach with respect to the v_v-fixed approach is then most probably because the w_v-component dominates the flow in the crosscut plane (y, z_v). As a result, the w_v-fixed approach provides a better description of the flow in that plane, which, in its turn, influences the secondary instability by determining the orientation of the secondary vortex cores (§ 8.5.2) and the distribution of the perturbing velocity component $\dot{v}_n$ normal to the unstable shear layer (§ 8.5.1).

9. Conclusions

Spatial DNS of secondary instability phenomena in a three-dimensional laminar boundary-layer flow obtained by perturbing single steady or unsteady CF modes have been carried out and compared with results from the secondary linear stability theory (SLST). The main results may be summarized as follows.

(*a*) The primary state for the SLST analysis is not uniquely defined by the underlying physical assumptions of the theory. We examined three equally legitimate procedures for extracting the primary state from the exact flow field and observed deviations in the resulting amplification rates of up to 50% with respect to the DNS. In all cases, the SLST underestimated the correct amplification rates from the DNS,

in particular for type I modes and with a marked sensitivity to modifications of the wall-normal and crossflow velocity components of the primary state.

(*b*) Perfect agreement was obtained between SLST and DNS when the primary state of the DNS was artificially modified to reproduce the simplified state of the SLST analysis (adapted DNS). This confirms the accuracy of the Gaster transformation proposed by Koch *et al.* (2000) and also provides a conclusive validation of the numerical procedures. The error in the amplification rates from the SLST is evidently due to the approximated representation of the primary state.

(*c*) Type I modes were found to be unstable both in steady and unsteady primary states. Type II modes were not observed in the DNS even if amplification was predicted by the SLST. However, unstable modes may be present but not visible in the DNS if they are covered by more unstable modes with the same frequency. SLST and DNS agree in predicting the amplification of type III modes in the steady fundamental case and their absence in the unsteady one.

(*d*) The inconsistency observed in the literature between experiment and SLST with respect to the role of type II modes is likely to be a consequence of inaccuracies in the SLST amplification rates. These may be due to the simplifications introduced by the theory, but also to inaccuracies in the primary state, to which SLST results have been found to be very sensitive. We find that SLST results considering the crosswise-velocity-w_v-fixed approach never show a dominance of type II modes, in agreement with the DNS. On the contrary SLST results obtained from the wall-normal-velocity-v_v-fixed approach indicate type II modes as the most amplified in the high-frequency range.

(*e*) The sensitivity of the secondary growth rates with respect to the small wall-normal and crossflow velocity components of the primary state opens a possibility for efficient transition control by moderate suction or blowing at the wall.

(*f*) Each local maximum of the secondary perturbation in the crosscut plane represents an eigenmode of the stability problem and develops independently from neighbouring maxima. This explains why spatial SLST results, where periodicity and exponential amplification are imposed respectively in the directions normal and parallel to the primary vortex-axis, may describe the infinite span configuration of the DNS, where periodicity and spatial amplification are assumed to be in the spanwise and chord directions, respectively. Indeed, neither the primary state nor the secondary perturbation need be periodic in any direction. A further consequence is that spanwise detuning in the sense of the Floquet theory is futile in the SLST of CF vortices. The tuned periodic problem and the detuned problem, considering, respectively, series of identical localized independent eigensolutions and spanwise modulated series of the same eigensolutions, both provide complete, and equivalent, information about the original localized eigensolution.

(*g*) Structures resulting from large-amplitude secondary modes have been documented and an analogy, unequivocal for type I and type II modes, with some deviations for type III modes, has been highlighted between the secondary CF instability and the inviscid Kelvin–Helmholtz instability of the plane mixing layer. Straightforward interpretations have been achieved for relevant aspects of the secondary instability. In particular, the strong sensitivity of secondary amplification rates with respect to the primary state has been found to be the transposition to the SLST case of the sensitivity of Kelvin–Helmholtz instabilities with respect to a velocity component normal to the unstable shear layer. The better performance provided by the w_v-fixed approach in predicting amplification rates for type I modes is most probably a consequence of the fact that the w_v-distribution determines that

normal component more directly than the v_v-distribution, it being understood that the shear layer is mainly determined by the gradient of u_r in the crosscut plane (y, z_r).

Partial financial support from 'Landesgraduiertenförderung Baden-Württemberg' within grant 7631.2-99/1 for G. B. is gratefully acknowledged. The authors would like to thank Dr R. Messing (Universität Stuttgart) for providing the SLST code and Dr W. Koch (DLR Göttingen) for providing his SLST code for validation.

REFERENCES

Balachandar, S., Streett, C. L. & Malik, M. R. 1992 Secondary instability in rotating-disk flow. *J. Fluid Mech.* **242**, 323–347.

Bippes, H. 1999 Basic experiments on transition in three-dimensional boundary layers dominated by crossflow instability. *Prog. Aerospace Sci.* **35**, 363–412.

Bonfigli, G. 2006 Numerical simulation of transition and early turbulence in a 3-d boundary layer perturbed by superposed stationary and traveling crossflow vortices. Dissertation, Universität Stuttgart.

Bonfigli, G. & Kloker, M. 1999 Spatial Navier–Stokes simulation of crossflow-induced transition in a three-dimensional boundary layer. In *New Results in Numerical and Experimental Fluid Mechanics II* (ed. W. Nitsche, H. J. Heinemann & R. Hilbig), *NNFM*, vol. 72. 11th AG STAB-DGLR Symposium, Berlin, Germany, 1998. Vieweg.

Chernoray, V. G., Dovgal, A. V., Kozlov, V. V. & Löfdahl, L. 2005 Experiments on secondary instability of streamwise vortices in a swept-wing boundary layer. *J. Fluid Mech.* **534**, 295–325.

Drazin, P. G. & Reid, W. H. 2004 *Hydrodynamic Stability*, 2nd edn. Cambridge University Press.

Hein, S. 2004 Nonlinear nonlocal transition ansalysis. Dissertation, Universität Stuttgart.

Högberg, M. & Henningson, D. 1998 Secondary instability of cross-flow vortices in Falkner–Skan–Cooke boundary layers. *J. Fluid Mech.* **368**, 339–357.

Janke, E. & Balakumar, P. 2000 On the secondary instability of three-dimensional boundary layers. *Theoret. Comput. Fluid Dyn.* **14**, 167–194.

Jeong, J. & Hussain, F. 1995 On the identification of a vortex. *J. Fluid Mech.* **285**, 69–94.

Kawakami, M., Kohama, Y. & Okutsu, M. 1999 Stability characteristics of stationary crossflow vortices in three-dimensional boundary layer. *AIAA Paper* 99-0811.

Kloker, M. 1993 Direkte Numerische Simulation des laminar-turbulenten Strömungsumschlages in einer stark verzögerten Grenzschicht. Dissertation, Universität Stuttgart.

Koch, W. 2002 On the spatio-temporal stability of primary and secondary crossflow vortices in a three-dimensional boundary layer. *J. Fluid Mech.* **456**, 85–111.

Koch, W., Bertolotti, F. P., Stolte, A. & Hein, S. 2000 Nonlinear equilibrium solutions in a three-dimensional boundary layer and their secondary stability. *J. Fluid Mech.* **406**, 131–174.

Lerche, T. 1997 Experimentelle Untersuchung nichtlinearer Strukturbildung im Transitionsprozeß einer instabilen dreidimensionalen Grenzschicht. Dissertation, Universität Göttingen.

Linnick, M. & Rist, U. 1999 Vortex identification and extraction in a boundary-layer flow. In *Vision, Modelling, and Visualization 2005* (ed. G. Greiner, J. Hornegger, H. Niemann & M. Stamminger), pp. 9–16. Akad. Verl.-Ges. Aka, November 16–18 2005. Erlangen, Germany.

Malik, M. R. & Chang, C. L. 1994 Crossflow disturbances in three-dimensional boundary layers: nonlinear development, wave interaction and secondary instability. *J. Fluid Mech.* **268**, 1–36.

Malik, M. R., Li, F., Choudhari, M. M. & Chang, C. L. 1999 Secondary instability of crossflow vortices and swept-wing boundary-layer transition. *J. Fluid Mech.* **399**, 85–115.

Messing, R. 2004 Direkte Numerische Simulationen zur diskreten Absaugung in einer dreidimensionalen Grenzschichtströmung. Dissertation, Universität Stuttgart.

Meyer, F. 1989 Numerische Simulation der Transition in dreidimensionalen Grenzschichten. Dissertation, Universität Göttingen.

Michalke, A. 1964 On the inviscid instability of the hyperbolic-tangent velocity profile. *J. Fluid Mech.* **19**, 543–556.

Michalke, A. 1982 On the inviscid instability of a circular jet with external flow. *J. Fluid Mech.* **114**, 343–359.

Müller, B. 1990 Experimentelle Untersuchung der Querströmungsinstabilität im linearen und nichtlinearen Bereich des Transitionsgebietes. Dissertation, Universität Göttingen.

Müller, W. 1995 Numerische Untersuchung räumlicher Umschlagvorgänge in dreidimensionalen Grenzschichtströmungen. Dissertation, Universität Stuttgart.

Radeztsky, R. H., Reibert, M. S. & Saric, W. S. 1999 Effect of isolated micro-sized roughness on transition in swept-wing flows. *AIAA J.* **38**, 1370–1377.

Reed, H. L. & Saric, W. S. 1989 Stability of three-dimensional boundary layers. *Annu. Rev. Fluid Mech.* **21**, 235–284.

Saric, W. S., Reed, H. L. & White, E. B. 2003 Stability and transition of three-dimensional boundary layers. *Annu. Rev. Fluid Mech.* **35**, 413–440.

Wassermann, P. & Kloker, M. 2002 Mechanisms and passive control of crossflow-vortex-induced transition in a three-dimensional boundary layer. *J. Fluid Mech.* **456**, 49–84.

Wassermann, P. & Kloker, M. 2003 Transition mechanisms induced by travelling crossflow vortices in a three-dimensional boundary layer. *J. Fluid Mech.* **483**, 67–89.

Wassermann, P. & Kloker, M. 2005 Transition mechanisms in a three-dimensional boundary-layer flow with pressure-gradient changeover. *J. Fluid Mech.* **530**, 265–293.

White, E. B. & Saric, W. S. 2005 Secondary instability of crossflow vortices. *J. Fluid Mech.* **525**, 275–308.

White, E. B., Saric, W. S., Gladden, R. D. & Gabet, P. M. 2001 Stages of swept-wing transition. *AIAA Paper* 2001-0271.

Wintergerste, T. 2002 Numerische Untersuchung der Spätstadien der Transition in einer dreidimensionalen Grenzschicht. Dissertation, Eidgenössische Technische Hochschule Zürich.